

# A foundation model utilizing chest CT volumes and radiology reports for supervised-level zero-shot detection of abnormalities

Ibrahim Ethem Hamamci<sup>1,2,†,\*</sup>, Sezgin Er<sup>3,†</sup>, Furkan Almas<sup>3</sup>, Ayse Gulnihan Simsek<sup>3</sup>, Sevval Nil Esirgun<sup>3</sup>, Irem Dogan<sup>3</sup>, Muhammed Furkan Dasdelen<sup>3</sup>, Bastian Wittmann<sup>1,2</sup>, Enis Simsar<sup>4</sup>, Mehmet Simsar<sup>3</sup>, Emine Bensu Erdemir<sup>3</sup>, Abdullah Alanbay<sup>3</sup>, Anjany Sekuboyina<sup>1</sup>, Berkan Lafci<sup>1</sup>, Mehmet K. Ozdemir<sup>3</sup>, and Bjoern Menze<sup>1,2</sup>

<sup>1</sup> Department of Quantitative Biomedicine, University of Zurich, Zurich, Switzerland

<sup>2</sup> ETH AI Center, ETH Zurich, Zurich, Switzerland

<sup>3</sup> International School of Medicine, Istanbul Medipol University, Istanbul, Turkey

<sup>4</sup> Department of Computer Science, ETH Zurich, Zurich, Switzerland

†These authors contributed equally to this work. \*Corresponding author: {ibrahim.hamamci@uzh.ch}

**Abstract.** A major challenge in computational research in 3D medical imaging is the lack of comprehensive datasets. Addressing this issue, our study introduces CT-RATE, the first 3D medical imaging dataset that pairs images with textual reports. CT-RATE consists of 25,692 non-contrast chest CT volumes, expanded to 50,188 through various reconstructions, from 21,304 unique patients, along with corresponding radiology text reports. Leveraging CT-RATE, we developed CT-CLIP, a CT-focused contrastive language-image pre-training framework. As a versatile, self-supervised model, CT-CLIP is designed for broad application and does not require task-specific training. Remarkably, CT-CLIP outperforms state-of-the-art, fully supervised methods in multi-abnormality detection across all key metrics, thus eliminating the need for manual annotation. We also demonstrate its utility in case retrieval, whether using imagery or textual queries, thereby advancing knowledge dissemination. The open-source release of CT-RATE and CT-CLIP marks a significant advancement in medical AI, enhancing 3D imaging analysis and fostering innovation in healthcare.

## 1 Introduction

Artificial intelligence (AI) has revolutionized the automatic interpretation of medical images [1–5]. Recent advances such as automated diagnosis, classification, and segmentation have been driven by numerous publicly available datasets [6–10]. In addition to these supervised methods, general AI systems have been developed, utilizing publicly available image-text pairs in self-supervised learning procedures, particularly in two-dimensional (2D) medical imaging [11, 12]. These versatile AI foundation models integrate comprehensive natural language annotations into the learning process and do not require task-specific training, eliminating the need for explicit manual image annotations. Moreover, these models are not constrained by predefined classes during training, elevating their adaptability to a multitude of tasks.

While significant advancements have been made in 2D medical imaging, the exploration of advanced AI techniques in three-dimensional (3D) medical imaging, such as computed tomography (CT), magnetic resonance imaging, and positron emission tomography, remains limited. A primary challenge lies in the scarcity of open-source 3D medical imaging datasets paired with textual reports or labels [13, 14]. Creating such datasets demands substantial resources, time, specialized domain knowledge, and technical expertise [15, 16]. Moreover, challenges arise from the increased computational requirements for 3D models [17, 18] and their limited open-source availability, especially concerning self-supervised learning, in comparison to their 2D counterparts. Previous studies have only touched the surface, with few exploring the field, including one that proposed supervised multi-abnormality detection for chest CT volumes [19]. However, this study’s limitations stem from its supervised training approach, which restricts it to a predefined number of abnormalities. Additionally, only a small portion of its dataset (3,630 chest CT volumes with multi-abnormality labels) has been made publicly available, and it lacks paired textual reports.

To address the challenges of advancing AI in 3D medical imaging, our study introduces the CT-RATE dataset, uniquely pairing chest CT volumes with radiology text reports. This dataset comprises 50,188 reconstructed non-contrast 3D chest CT volumes from 25,692 distinct CT experiments conducted on 21,304 unique patients. Alongside the corresponding reports, each volume is annotated with 18 distinct types of abnormalities, facilitating further experiments in validation and fine-tuning. To promote further research, we make CT-RATE fully open-source, making it the only publicly available 3D medical imaging dataset paired with reports and the largest chest CT dataset with multi-abnormality labels. Then, leveraging the CT-RATE dataset, we develop CT-CLIP, a novel chest CT-focused contrastive language-image

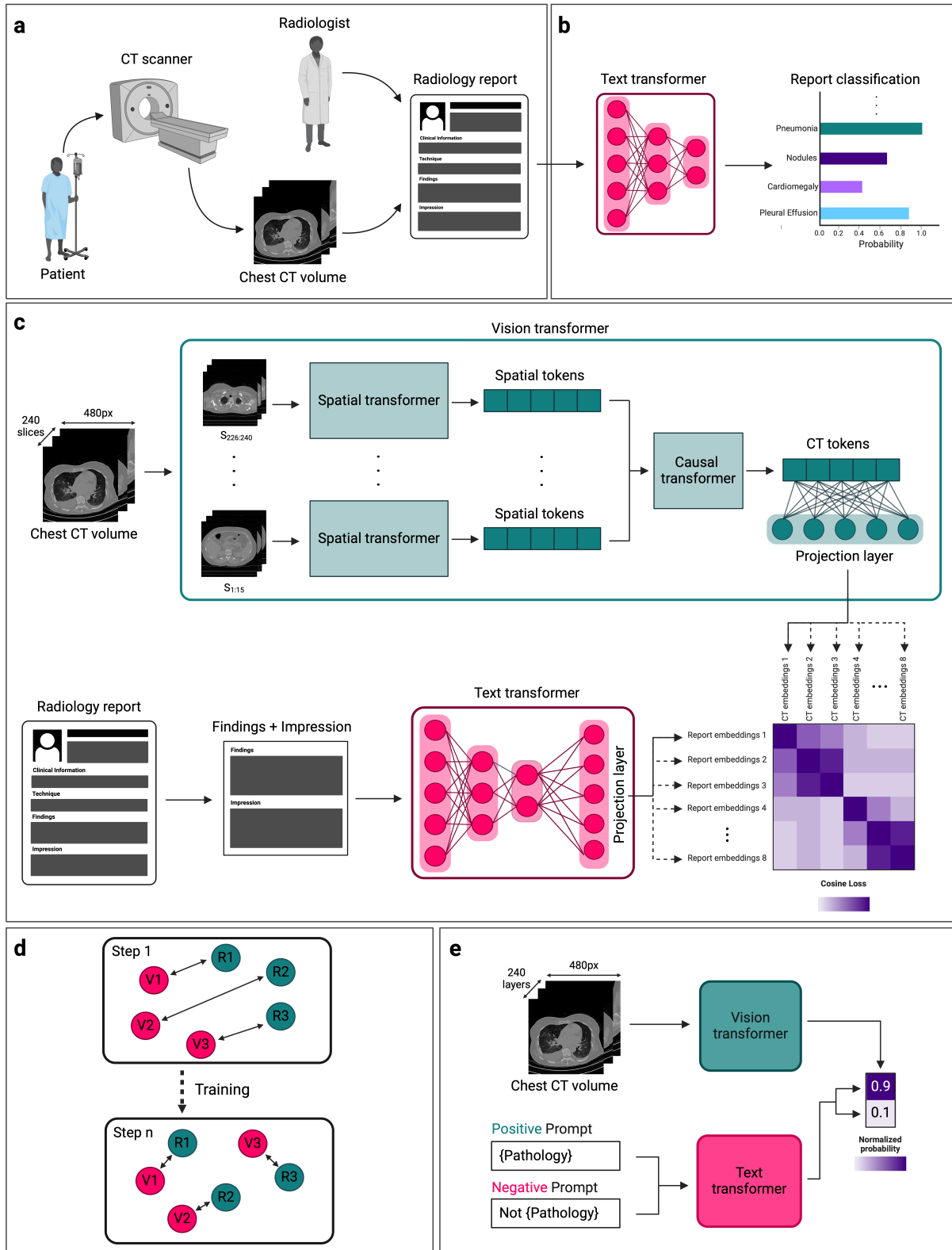


**Figure 1: Overview of our dataset and method.** **a.** Data acquisition protocol for the CT-RATE dataset, comprising non-contrast 3D chest CT volumes and corresponding radiology text reports written by expert radiologists. **b.** Extraction of multi-abnormality labels from radiology reports using a fine-tuned text encoder. **c.** Training of our CT-CLIP framework, which pairs chest CT volumes with radiology reports from the CT-RATE dataset through a contrastive learning approach. **d.** Illustration of the contrastive learning procedure, employed in the correlation matrix during training to ensure precise match recognition and mismatch differentiation. **e.** Inference for zero-shot multi-abnormality detection, where the binary label for each abnormality is determined by selecting the prompt with the highest cosine similarity.

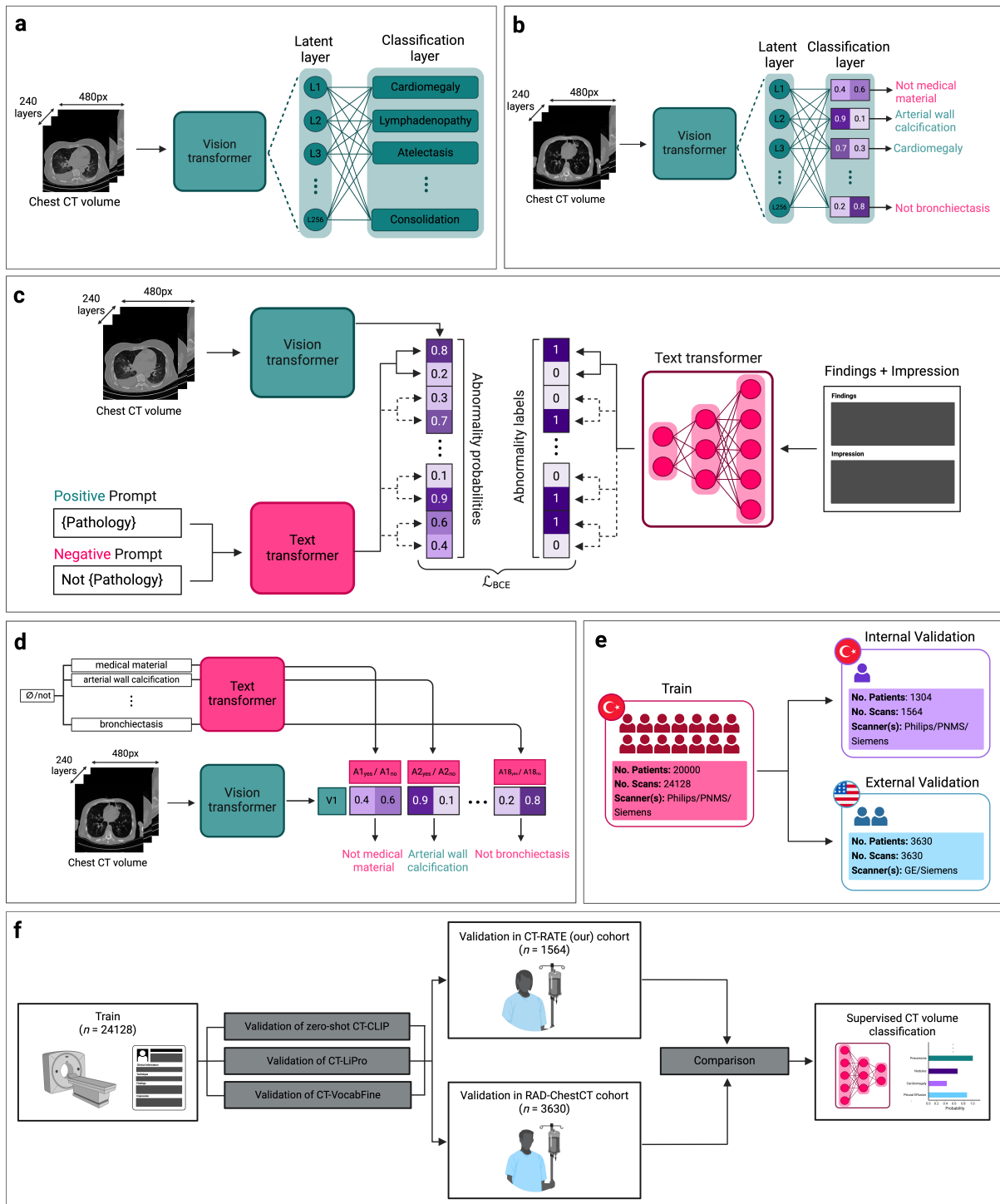


**Figure 2: Fine-tuning of CT-CLIP and the validation strategy.** **a.** Illustration of linear probing fine-tuning (CT-LiPro) for CT-CLIP, incorporating a linear layer into the vision encoder. **b.** CT-LiPro facilitates multi-abnormality classification restricted to classes predefined during fine-tuning. **c.** Process of the CT-CLIP's open vocabulary fine-tuning (CT-VocabFine) for each abnormality. **d.** CT-VocabFine allows for open vocabulary abnormality classification, even after fine-tuning. **e.** Training of each model on the CT-RATE dataset from Turkey, followed by evaluation on both an internal CT-RATE dataset and an external dataset from the US; detailed analysis of the CT-RATE dataset is presented in Figure 3. **f.** A comprehensive performance evaluation of zero-shot CT-CLIP and the two distinct fine-tuned models on two different cohorts, compared with a fully supervised method in a multi-abnormality detection task.

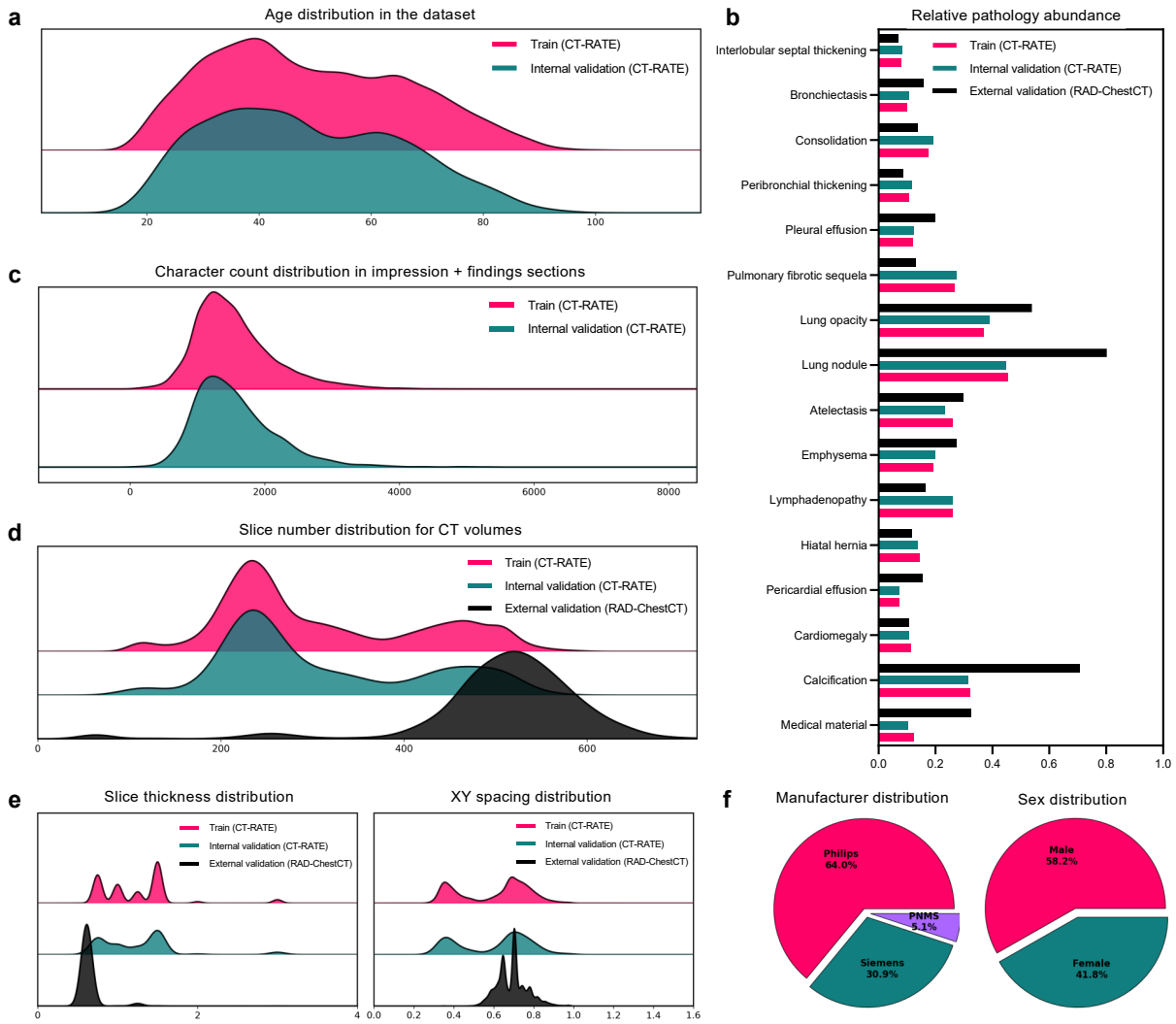


**Figure 3: Comprehensive analysis of the novel CT-RATE dataset.** **a.** CT-RATE comprises data from 21,304 unique patients, with ages ranging from 18 to 102 years. **b.** For validation and fine-tuning purposes, multi-abnormality labels for 18 distinct abnormalities are extracted from the corresponding radiology reports for each CT volume. **c.** The training process of the CT-CLIP model utilizes the *impression* and *findings* sections of radiology reports, which vary in length, along with the chest CT volumes. **d.** The number of slices in the chest CT volumes within CT-RATE ranges from 100 to 600. **e.** Spacings in the x-axis, y-axis, and z-axis vary across volumes; all chest CT volumes are preprocessed to ensure consistent spacing before training each model. **f.** Despite originating from a single institution, CT-RATE includes volumes acquired using scanners from three different manufacturers, ensuring variability.

pre-training framework. CT-CLIP integrates extensive natural language annotations into the learning process, enabling the model to comprehend image-based semantic knowledge and perform various tasks.

Our study makes several pivotal contributions to 3D medical imaging and AI. First, we address the scarcity of open-source 3D medical imaging datasets by introducing CT-RATE. Second, we create CT-CLIP, a novel and versatile foundation model that effectively integrates linguistic and visual data from CT-RATE via contrastive learning [20]. Third, we demonstrate CT-CLIP’s remarkable adaptability and performance across a variety of tasks without task-specific training. Our evaluation shows CT-CLIP’s ability to detect multiple abnormalities in a zero-shot setting [21], outperforming the state-of-the-art fully supervised method across all key metrics, on two test sets from different countries. These findings indicate that, given the availability of corresponding radiology reports, explicit labels are not essential for achieving high performance in 3D medical imaging interpretation. Additionally, two distinct fine-tuning techniques exhibited superior performance, thereby establishing CT-CLIP as a successful image encoder. Lastly, we demonstrate CT-CLIP’s ability to retrieve relevant CT volumes using text or volume

inputs, potentially becoming an essential educational and knowledge-sharing tool for clinicians [22]. These contributions address critical challenges in dataset scarcity, model versatility, and learning paradigms in 3D medical imaging, leading to groundbreaking research and substantial advancements in the field.

## 2 Results

### 2.1 Creating a novel dataset pairing chest CT volumes with radiology reports

We have curated and open-sourced a novel dataset, CT-RATE, which comprises 3D chest CT volumes and their corresponding radiology text reports from a cohort of 21,304 unique patients (Fig. 1a). CT-RATE includes 25,692 non-contrast 3D chest CT volumes, reconstructed using multiple methods suitable for various window settings [23], amounting to a total of 50,188. This dataset has been processed and divided into training and internal validation sets, as detailed in the methods section. To comprehensively evaluate our models’ performance under distribution shifts, we incorporated an external validation set, RAD-ChestCT, from a cohort of an independent study originating from a different country [19].

Figure 3 provides a detailed summary of CT-RATE, divided into training and internal validation sets, along with the external validation dataset, RAD-ChestCT, used in subsequent experiments. Figure 3a illustrates the age distribution within these sets, while Figure 3b presents the abnormality distributions. Additionally, Fig. 3c displays the length distribution of the findings and impression sections used for training CT-CLIP, which are only available for CT-RATE due to the absence of radiology reports in RAD-ChestCT. Figure 3d provides the distribution of slice numbers in CT volumes, and Figure 3e highlights variations in slice thickness and XY spacing. Lastly, Fig. 3f depicts the distribution of CT manufacturers and the patients’ sex. Supplementary Table 1 provides the exact numbers of abnormalities, manufacturers, and sex distributions in the training and internal validation sets, along with their ratios.

### 2.2 Extracting abnormality labels from radiology text reports

Conventional supervised machine learning approaches for medical image classification tasks necessitate manual annotation of large datasets, a process that is time-intensive and requires significant expertise [24]. Although our contrastive learning approach, CT-CLIP, does not require abnormality labels, the baseline supervised model and fine-tuning methods do. To meet this need, we utilized an automated text classifier to extract abnormality labels from radiology reports (Fig. 1b). This process involved fine-tuning a pre-trained language model, RadBERT [25], aligning with recent trends [26]. Within the CT-RATE dataset, we manually annotated 1,000 radiology reports for 18 distinct abnormalities for this fine-tuning procedure. The fine-tuned model’s precision, recall, and F1 scores, detailed in Supplementary Table 2, show robust classification across abnormalities, ensuring the CT-RATE dataset is enriched with high-quality labels.

### 2.3 CT-RATE enables developing a visual-language foundational model

Unlike other methods utilizing supervised machine learning for multi-abnormality classification of CT volumes, our study employs radiology reports, which provide a rich source of semantic knowledge. This significantly enhances understanding of CT volumes and supports a wide range of potential zero-shot applications. Accordingly, we developed CT-CLIP, the first foundational model for chest CT-focused, contrastive language-image pre-training, adapting a technique from a previous study [27]. We utilized the impression and findings sections of radiology reports for CT-CLIP due to their superior performance, as demonstrated by the abnormality classification scores in an ablation study (Supplementary Figure 1a).

CT-CLIP comprises a vision transformer and a text transformer that generate two distinct embedding vectors: one for CT volumes and another for radiology reports, respectively. CT-CLIP is then trained to ensure similarity between these vectors for volume-text pairs while maintaining dissimilarity for unpaired ones. This training employs cosine loss via contrastive learning [28] (Fig. 1c and Fig. 1d). This method enables the training of a foundational model suitable for various applications without task-specific training, including multi-abnormality classification, volume-to-volume retrieval, and report-to-volume retrieval.

Subsequent sections demonstrate how CT-CLIP can be applied to these downstream tasks without additional training. We also explore fine-tuning methods for the classification task to achieve greater accuracy. To analyze the latent spaces of radiology reports and CT volumes generated by CT-CLIP, we computed t-SNE embeddings of these spaces. Figure 4d shows the distribution according to the number of abnormalities present in a case. Figure 4e differentiates all cases, based on the presence of at least one abnormality. The well-clustered t-SNE embeddings for these abnormality groups confirm CT-CLIP’s ability to accurately represent the latent spaces. Extended Data Figures 1-2 provide additional t-SNE plots for each abnormality using volume and report embeddings, respectively.

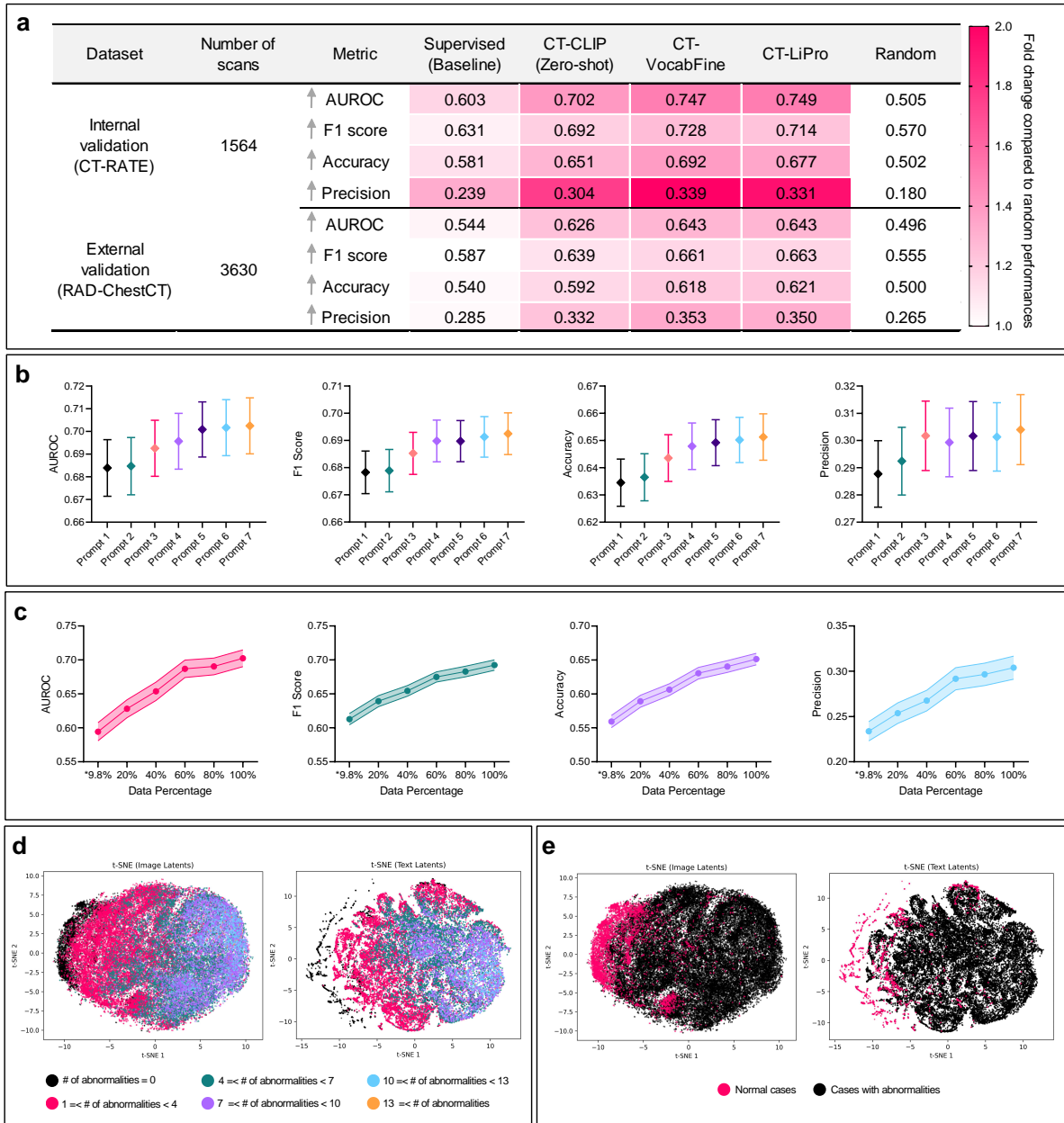


**Figure 4: A detailed evaluation of our method a.** Multi-abnormality classification performance is evaluated on both internal and external validation sets using four key metrics. Our zero-shot CT-CLIP method outperformed the fully supervised baseline across all metrics. Performance improved with both fine-tuning techniques, demonstrating the robustness of the CT-CLIP encoder in feature extraction from CT volumes. The scores are color-highlighted to emphasize the performance increase compared to random benchmarks. **b.** We utilized various prompts for the zero-shot multi-abnormality detection task with CT-CLIP. The best-performing prompt, emphasizing the importance of prompt engineering, was chosen for further experiments. **c.** To illustrate how large datasets enhance performance, we trained CT-CLIP using different portions of CT-RATE. (9.8% of CT-RATE matches the size of the only currently available open-source chest CT dataset with multi-abnormality labels.) Contour lines denote  $\pm 1$  standard deviations calculated via bootstrapping. **d.** t-SNE plots map the distributions of the number of abnormalities present in a case, utilizing the latent values from individual reports and CT volumes in CT-RATE. **e.** The t-SNE plots are binary-colored to indicate whether a case has at least one abnormality or none at all.

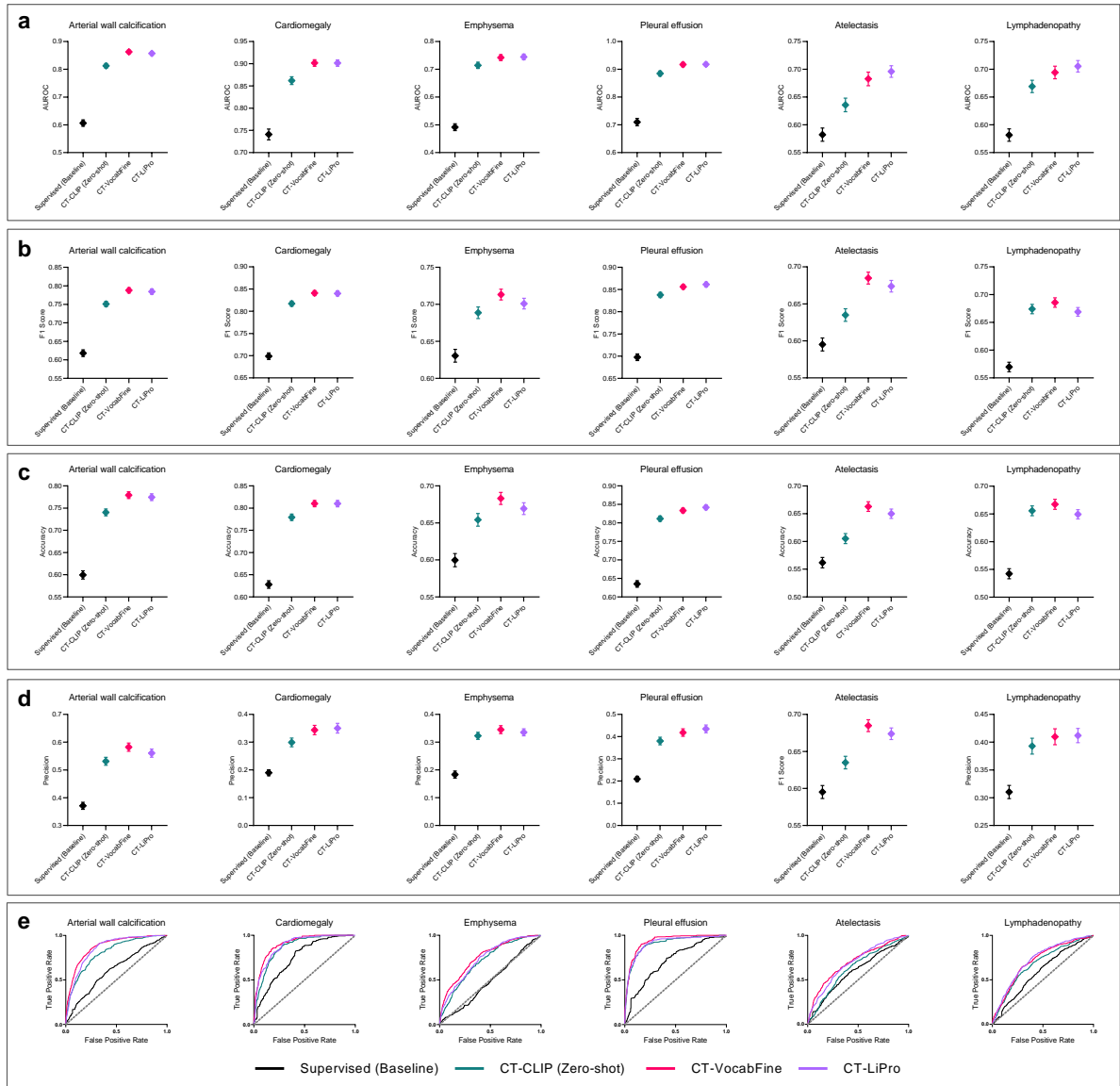


**Figure 5: Comparisons of abnormality-based performance metrics.** **a.** Abnormality-based AU-ROCs for six classes, showing the zero-shot CT-CLIP model outperforming the fully supervised baseline, with both fine-tuning methods enhancing performance. **b.** F1 scores comparison underscores CT-CLIP’s effectiveness and the utility of leveraging radiology reports. Notably, CT-LiPro fine-tuning decreases the lymphadenopathy score, suggesting the need for further investigation. **c.** Accuracy comparisons reveal that zero-shot CT-CLIP surpasses the supervised baseline across all abnormalities, with both fine-tuning further improving scores. However, as with the F1 score, fine-tuning with CT-LiPro diminishes accuracy for lymphadenopathy. **d.** Precision comparisons again show zero-shot CT-CLIP’s superiority over the supervised baseline, with both fine-tuning methods enhancing performances. **e.** ROC curve comparisons for all four models indicate that zero-shot CT-CLIP consistently outperforms the supervised baseline across abnormalities. Fine-tuning techniques, however, do not significantly boost CT-CLIP’s performance.

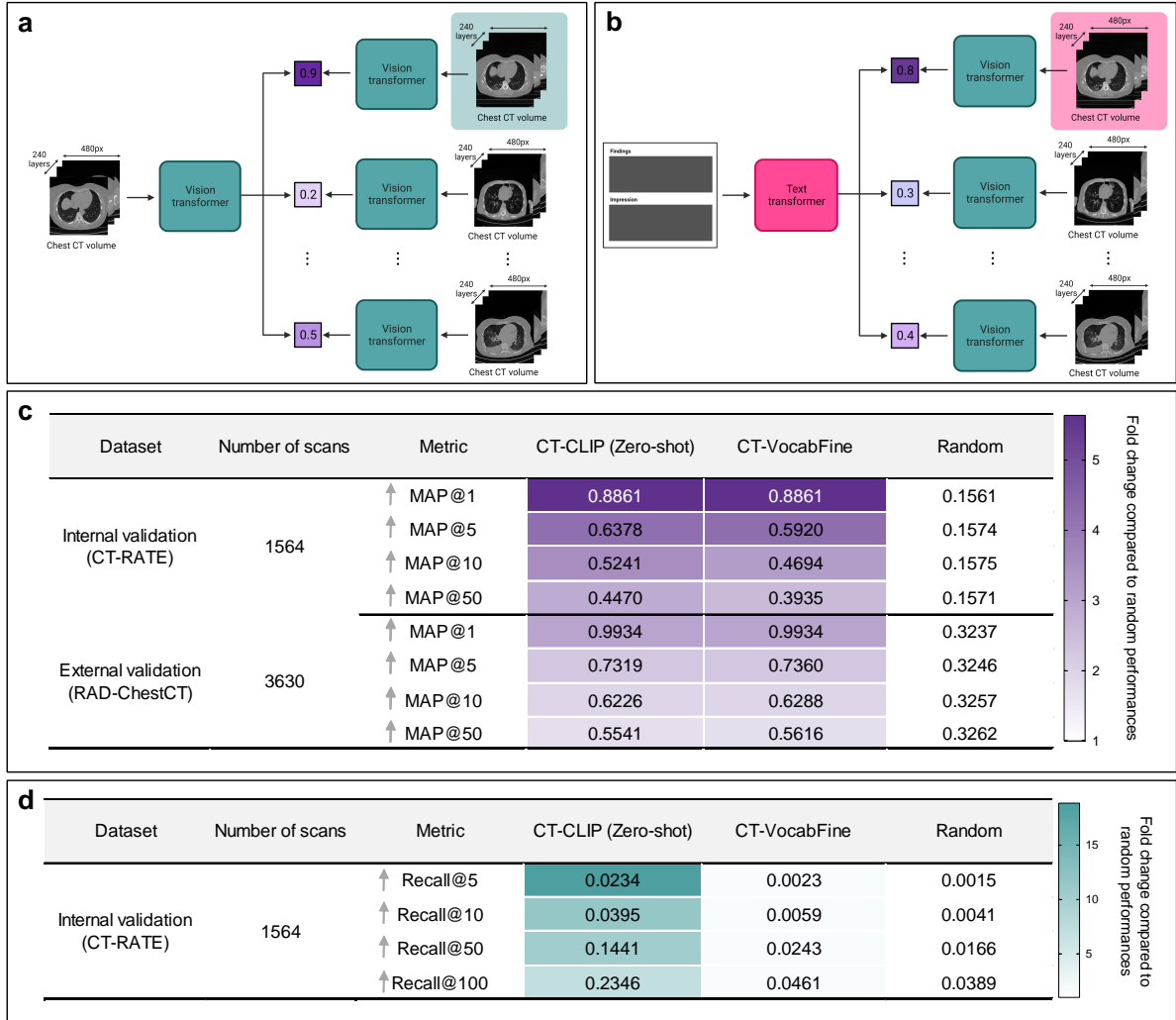


**Figure 6: Utilizing CT-CLIP for retrieval of chest CT volumes** **a.** Illustration of volume-to-volume retrieval facilitated by CT-CLIP’s vision transformer. **b.** Illustration of report-to-volume retrieval utilizing both vision and text transformers within CT-CLIP. **c.** Comprehensive evaluation of volume-to-volume retrieval performance on internal and external validation sets, with scores color-highlighted to emphasize improvements over random scores. **d.** An in-depth evaluation of report-to-volume retrieval performance, limited to the internal validation set due to the absence of paired radiology reports in the external set. Notably, fine-tuning CT-CLIP for classification tasks diminishes its retrieval performance. This reduction in performance is primarily observed in report-to-volume retrieval, indicating that the CT-VocabFine fine-tuning predominantly impacts the text transformer component of CT-CLIP.

## 2.4 Setting a supervised baseline for benchmarking CT-CLIP

To assess CT-CLIP’s zero-shot multi-abnormality classification performance, we compared it against CT-Net [19], the state-of-the-art fully supervised model for chest CT volumes, serving as our baseline (Fig. 2d). CT-Net necessitates manual annotation for each abnormality type due to its supervised nature, demanding considerable time and domain expertise [29]. Our primary aim in selecting CT-Net as the baseline was to demonstrate that our zero-shot CT-CLIP model can achieve even superior classification performance without depending on manual annotations and without being limited to predefined classes.

Figure 4a illustrates CT-Net’s performance with key metrics such as average AUROC, F1 score, accuracy, and precision, evaluated on both internal and external validation datasets. Furthermore, Fig. 5a-d provides a detailed breakdown of these metrics, while Fig. 5e displays the ROC curves for specific abnormalities. Extended Data Figures 3 and 4 present classification scores for each abnormality on the internal and external validation sets, respectively. Supplementary Figures 2 and 6 show confusion matrices



for each abnormality on the internal and external validation sets, respectively. Despite utilizing a different dataset, the classification scores of CT-Net are comparable to those reported in the original study [19].

## 2.5 CT-CLIP enables zero-shot multi-abnormality detection surpassing supervised levels

Zero-shot classification with foundational models is typically implemented as a multi-class classification task, assigning a single label to each image [27]. However, medical images may present multiple abnormalities, necessitating a unique approach. Inspired by recent work on 2D chest radiographs [11], we created both positive and negative prompts for each abnormality and computed the cosine similarity loss between these prompts’ embeddings and the input CT volume. We then applied a softmax operation to the logits generated by both prompts, converting the model’s logit outputs into probabilities. We retained the softmax probabilities derived from the positive logits to indicate the likelihood of each abnormality’s presence in the CT volume, as shown in Fig. 1e. We then conducted a systematic evaluation of CT-CLIP’s zero-shot classification capabilities on both internal and external validation datasets (Fig. 4a).

Our zero-shot approach yields significantly higher mean AUROC (0.099 higher in internal validation and 0.082 higher in external validation), mean F1 score (0.061 higher in internal validation and 0.052 higher in external validation), mean accuracy (0.07 higher in internal validation and 0.052 higher in external validation), and mean precision (0.065 higher in internal validation and 0.047 higher in external validation) compared to the supervised baseline. These results demonstrate that the model not only performs better within similar data distributions but also under distribution shifts, showing it generalizes well to external data. A two-sided paired permutation test, utilizing 1,000 permutations, highlights statistically significant improvements ( $p < 0.05$ ) in AUROC, F1 score, and accuracy for the CT-CLIP (zero-shot) model over the supervised (baseline) model, detailed in Supplementary Table 4.

Figure 5a-d displays abnormality-specific AUROC, F1 score, accuracy, and precision for selected abnormalities, and Fig. 5e presents ROC plots for these abnormalities. Extended Data Figures 3 and 4 provide scores for all abnormalities on the internal and external validation sets, respectively. Supplementary Figures 3 and 7 show confusion matrices on the internal and external validation sets, respectively. Notably, on the internal validation set, 17 out of 18 abnormalities exhibit higher scores in zero-shot CT-CLIP compared to the supervised baseline, except for lung opacity showing minimal change ( $< 0.01$ ) in mean AUROC. In conclusion, CT-CLIP excels by just leveraging existing text reports in electronic health records, thus avoiding the need for expensive manual annotations. Moreover, it offers flexible predictions beyond predefined classes and adapts efficiently to changing needs post-training.

## 2.6 Prompt engineering enhances classification performance

The careful engineering of prompts is crucial in zero-shot classification tasks with foundational models, as it significantly impacts performance [30]. Therefore, we evaluated seven distinct prompts commonly used in reports, with detailed information provided in the online methods section. Figure 4b presents the mean AUROC, F1 score, accuracy, and precision for these various prompts. For the experiments with CT-CLIP, we selected prompt 7 ( $\{\emptyset/Not\} \{abnormality\}$ .) due to its superior performance.

## 2.7 Larger datasets yield enhanced classification performance

The availability of sufficiently large datasets is crucial for machine learning, especially for transformer models, which require more data than convolutional neural networks [31, 32]. Here, we demonstrate the impact of dataset size on classification performance. We trained CT-CLIP on different portions of the CT-RATE dataset, specifically 9.8% (equivalent to the open-source portion of the RAD-ChestCT dataset [19]), 20%, 40%, 60%, 80%, and 100%. Figure 4c illustrates the classification performance across different dataset sizes. Notably, a consistent trend emerges: larger dataset sizes correlate with improved scores. This finding highlights the role of dataset size in enhancing CT-CLIP’s zero-shot classification performance and underscores the value of our extensive CT-RATE dataset for computational research.

## 2.8 Open vocabulary fine-tuning of CT-CLIP

To enhance the classification performance of CT-CLIP, we developed a novel open vocabulary fine-tuning method, CT-VocabFine, inspired by the WISE-FT, a robust fine-tuning approach of zero-shot models for multi-class classification [33]. CT-VocabFine, similar to the multi-label zero-shot inference approach

of CT-CLIP, is fine-tuned to improve accuracy in predicting classification labels (Fig. 2c). The open-vocabulary inference with CT-VocabFine, depicted in Fig. 2d, is the same as the original CT-CLIP. Figure 4a highlights the improved classification scores achieved by CT-VocabFine compared to zero-shot CT-CLIP. These enhancements are evident in the mean AUROC (0.045 higher in internal validation and 0.017 higher in external validation), F1 score (0.036 higher in internal and 0.022 higher in external validation), accuracy (0.041 higher in internal and 0.026 higher in external validation), and precision (0.035 higher in internal and 0.021 higher in external validation) across both validation sets. Specific abnormalities are highlighted in Fig. 5, showing the AUROC, F1 score, accuracy, and precision values. Extended Data Figures 3 and 4 provide scores for the remaining abnormalities on internal and external validation sets, respectively. Notably, fine-tuning the zero-shot model improved classification scores for all 18 abnormalities on the internal validation set. Supplementary Figure 1b illustrates the impact of training only the projection layers versus training all weights during fine-tuning, underscoring the importance of comprehensive training. Supplementary Figures 4 and 8 show confusion matrices for each abnormality on internal and external validation sets, respectively, providing further insight into the method.

## 2.9 Fine-tuning CT-CLIP with linear probing

To enhance the classification performance and demonstrate the effectiveness of our open vocabulary fine-tuning approach, we implemented another task-specific fine-tuning method, inspired by the conventional linear probing technique. CT-LiPro involves adding a new classification layer to the vision transformer component of CT-CLIP (Fig. 2a). Supplementary Figure 1b explores the impact of training only the last layer compared to training all weights, highlighting the sufficiency of training only the last classification layer for fine-tuning. The inference process of CT-LiPro, demonstrated in Fig. 2b, aligns with that of supervised methods. Figure 4a showcases the enhanced classification scores achieved by CT-LiPro over CT-CLIP, including higher mean AUROC (0.047 in internal and 0.017 in external validation), F1 score (0.022 in internal and 0.024 in external validation), accuracy (0.026 in internal and 0.029 in external validation), and precision (0.027 in internal and 0.018 in external validation). Figure 5a-d presents the AUROC, F1 score, accuracy, and precision values for specific abnormalities. Extended Data Figures 3 and 4 provide scores for all abnormalities on internal and external validation sets, respectively. Supplementary Figures 5 and 9 show confusion matrices on the internal and external validation sets, respectively. Notably, similar to CT-VocabFine, CT-LiPro fine-tuning improved classification scores across all abnormalities compared to CT-CLIP. Against CT-VocabFine, it showed comparable performance for most abnormalities (10 out of 18) with less than a 0.01 change in AUROC. Given that fine-tuning with CT-LiPro restricts the model to predefined labels, limiting its applicability to other downstream tasks such as case retrieval, these comparable performances underscore the value of our open vocabulary fine-tuning method.

## 2.10 CT-CLIP enables volume-to-volume retrieval

Besides zero-shot classification, CT-CLIP serves as a powerful tool for volume-to-volume retrieval, similar to image-to-image retrieval [34], enabling the identification of the most relevant volumes from an input volume. This method compares the cosine similarities between the embeddings of query and candidate volumes (Fig. 6a). Utilizing the vision transformer components of both CT-CLIP and CT-VocabFine, we conducted tests on both internal and external validation sets. To assess accuracy, we utilized the Mean Average Precision at K (MAP@K) metric, where K represents the number of returned images, for an effective evaluation of the similarity between the query volume and the retrieved volumes. We calculated MAP@1, MAP@5, MAP@10, and MAP@50 to assess performance. Notably, as K increases, the MAP@K score typically decreases due to the inclusion of less accurate matches.

Volume-to-volume retrieval results, summarized in Fig. 6c, reveal that on the internal validation set, CT-VocabFine performs comparably to CT-CLIP, with both models significantly outperforming random retrieval (about six times higher at MAP@1). On the external validation set, although MAP@K scores are higher compared to the internal set (e.g., 0.9934 vs. 0.8861 at MAP@1), the fold increase over random retrieval is lower (three times on the external versus six times on the internal set). This discrepancy could be due to the differing abnormality distributions in the datasets, which influence the MAP@K scores. Thus, examining the fold change provides a more accurate comparison. Both CT-CLIP and CT-VocabFine demonstrated similar performance across the MAP@K metrics, indicating that fine-tuning with CT-VocabFine does not significantly alter the weights of CT-CLIP’s vision transformer.

### 2.11 CT-CLIP enables report-to-volume retrieval

CT-CLIP also excels as a report-to-volume search tool, similar to text-to-image retrieval [35], by evaluating the cosine similarity between the embeddings of target volumes and the embeddings from query texts (Fig. 6b). Due to the limitations of the supervised model and CT-LiPro in encoding text, we exclusively employed CT-CLIP and CT-VocabFine for our experiments. Since the RAD-ChestCT dataset lacks radiology reports, we only utilized the internal validation set for report-to-volume retrieval.

To assess performance, we employed Recall@K, where K denotes the number of returned images, measuring the percentage of correctly corresponding images for the query text within the top K-returned images. While the Recall@K score increases with the number of volumes returned, it's crucial to consider that the random value for Recall@K also increases with larger K values. Thus, calculating the fold change relative to random performance provides a more meaningful comparison. Figure 6d presents the Recall@5, Recall@10, Recall@50, and Recall@100 scores for both the zero-shot CT-CLIP and CT-VocabFine models. Notably, these scores were significantly higher than the random baseline, exceeding a 15-fold increase for CT-CLIP. However, the Recall@K scores for CT-VocabFine were substantially lower than those for CT-CLIP, consistent with the expectation that fine-tuning a foundational model for a specific task might diminish its efficacy for other tasks. The reduced performance of CT-VocabFine in the report-to-volume retrieval task further indicates significant modifications to the text transformer weights due to fine-tuning.

## 3 Discussion

Recent machine learning advancements have greatly improved the automatic interpretation of 2D medical images [36], driven by publicly available annotated datasets [37]. However, the progress in applying these advances to 3D medical images, which are crucial for health care, is hindered by the scarcity of open-source datasets, which are costly and labor-intensive to annotate, necessitating extensive domain expertise [38].

Radiology reports encapsulate a radiologist's insights into a patient's condition based on medical images [39]. These reports are invaluable for machine learning, providing comprehensive descriptions of medical images without adding extra labeling burden, as they are already part of the daily routine for radiologists. Recent studies show that foundational models, trained on paired text reports and 2D medical images, perform comparably to fully supervised methods in various tasks [11]. However, these studies have not extended to 3D medical imaging, where 3D images provide more and better diagnostic information than their 2D counterparts, primarily because a publicly available 3D medical imaging dataset paired with reports is absent. Therefore, CT-RATE, which pairs chest CT volumes with radiology text reports (Fig. 1a), represents a significant advancement as the first of its kind. In this study, we introduce this novel and comprehensive dataset and utilize it to develop CT-CLIP (Fig. 1c). To our knowledge, CT-CLIP is the first self-supervised learning model in 3D medical imaging utilizing radiology text reports.

CT-CLIP offers a general solution applicable to various tasks without requiring task-specific training. Unlike supervised methods, our approach saves considerable effort by not requiring explicit labels and by enabling predictions beyond predefined classes (Fig. 1e). This flexibility in handling a variety of classes is particularly valuable when learning objectives evolve post-training. Additionally, our zero-shot CT-CLIP model outperforms the state-of-the-art supervised method for the multi-abnormality detection task on the internal validation set across all metrics (Fig. 4a). This demonstrates that explicit labels are not mandatory for high performance in 3D medical image interpretation tasks when corresponding reports are available for training. Furthermore, we externally validated zero-shot CT-CLIP on an independent dataset, Rad-ChestCT, from a different country (Fig. 2e). The model's ability to generalize to different data distributions, a primary challenge in deploying medical AI [40], was confirmed as it outperformed the fully supervised method in all metrics in the external validation set as well (Fig. 4a).

To establish a fully supervised baseline for comparison and fine-tuning CT-CLIP, we extracted multi-abnormality labels from radiology reports, making them publicly available as well. Following recent trends, we developed an automatic label extractor by fine-tuning a language model (Fig. 1b) [41]. However, creating such a system demands significant time, technical expertise, and domain knowledge, as evidenced by our substantial effort in manually annotating a portion of the reports. CT-CLIP addresses this bottleneck by classifying abnormalities at a supervised level without the need for automatic labeler development. Consequently, it overcomes a major barrier in 3D medical image research, achieving superior performance through readily available reports in electronic health records, thus eliminating the need for costly manual annotations. In fine-tuning experiments, CT-CLIP's robust representational learning capabilities were confirmed by both methods (Fig. 2a-d), demonstrating superior performance (Fig. 4a).

Despite their breakthroughs, our unique CT-RATE dataset and novel CT-CLIP model have limitations. For example, biases in our single-institution dataset may have influenced the performance of our

self-supervised method. Additionally, if a report never mentions an abnormality, the method may not accurately predict that pathology during the zero-shot evaluation. To mitigate potential biases, we collected a large set of volume-report pairs for training and conducted an ablation study to assess the impact of training set size on CT-CLIP’s performance. This study revealed an almost linear performance increase with larger training sets (Fig. 4c), indicating the potential benefit of a more extensive training dataset. This ablation study also underscores the value of our large and unique CT-RATE dataset. Another limitation is CT-CLIP’s dependency on the terminology used in the reports and the choice of prompts during inference, as the same disease can be described differently. To assess the importance of prompt engineering, we evaluated the zero-shot multi-abnormality detection performance using seven different prompts during inference (Fig. 4b). While we selected the best-performing prompt from commonly used structures in radiology reports, continued optimization of prompts may further improve performance.

As another application of CT-CLIP, we showcased its retrieval capabilities (Fig. 6a-b), highlighting its potential as a search tool within large hospital databases (Fig. 6c-d). Notably, fine-tuning with CT-VocabFine does not affect volume-to-volume retrieval performance but decreases report-to-volume performance, suggesting that fine-tuning primarily alters the weights of the text encoder rather than the image encoder. Additionally, effective clustering in t-SNE plots (Fig. 4d-e) unveils another intriguing aspect and potential clinical application of CT-CLIP. Given the successful clustering of abnormalities (Extended Data Fig. 1 and 2), CT-CLIP could extend its utility beyond multi-abnormality detection, potentially assisting in prognosis, disease grading, and calculation of lung-related variables.

In conclusion, the development of the CT-CLIP model represents a significant breakthrough in medical imaging, particularly for interpreting chest CT volumes. This achievement was made possible by compiling CT-RATE, the first 3D medical image dataset, paired with corresponding radiology text reports. The open-source availability of both CT-CLIP and CT-RATE is expected to be a substantial asset to the medical AI community, providing a solid foundation for further advancements in 3D medical imaging. Moreover, CT-CLIP accelerates the dissemination of medical knowledge through its role as a retrieval tool, marking a stride in integrating AI-driven tools into medical research and practice.

## 4 Online Methods

### 4.1 Ethics statement

Our study received ethical approval from the Clinical Research Ethics Committee at Istanbul Medipol University (E-10840098-772.02-6841, 27/10/2023) for the open-sourcing of our CT-RATE dataset and associated trained models. To uphold patient privacy, we rigorously anonymized all chest CT volumes, associated metadata, and radiology text reports before conducting any computational analysis.

### 4.2 Creating the CT-RATE dataset

**4.2.1 Description of the CT-RATE dataset** We curated a novel dataset, CT-RATE, comprising chest CT volumes and corresponding radiology text reports from Istanbul Medipol University Mega Hospital. The CT-RATE dataset includes non-contrast chest CT volumes acquired between May 2015 and January 2023, totaling 50,188 reconstructed CT volumes from 25,692 distinct CT experiments conducted on 21,304 unique patients. The sample size was based on all available data in the database. We divided the cohort into two groups: 20,000 patients were allocated to training and 1,304 for validation. Figure 1a illustrates the dataset accumulation process, and Fig. 2e shows the training and validation split.

In clinical practice, CT volumes are reconstructed with various techniques to meet specific diagnostic requirements. Sharper kernels, for instance, improve resolution for lung abnormalities, whereas smoother kernels are favored for assessing mediastinal issues [23]. To accommodate differences in spatial resolution and image noise resulting from diverse reconstruction methods, we incorporated every reconstructed volume from the hospital database into our dataset. This strategy facilitates a thorough evaluation of various abnormalities, mirroring the range of imaging techniques employed in clinical environments.

The patients ranged in age from 18 to 102 years, with a mean of 48.8 years and a mode of 40 years. The sex distribution was 41.6% female and 58.4% male. Regarding the scanners, 61.5% of the scans were performed using Philips CT scanners, 30.1% with Siemens scanners, and 8.4% with PNMS (Philips-Neusoft Medical Systems) scanners. The CT volumes were provided in various resolutions: 65.4% in  $512 \times 512$  px, 4.2% in  $768 \times 768$  px, and 30.4% in  $1024 \times 1024$  px. The number of slices per volume ranged from 100 to 600, averaging 304.7 with a mode of 255 slices, demonstrating variability in interslice spacing.

The radiology reports are structured into four sections: clinical information, technique, findings, and impression. The clinical information section outlines the patient’s symptoms and medical history. The

technique section specifies the image acquisition protocol, encompassing details such as the field of view and the administration of IV contrast material. The findings section covers anatomical and pathological observations, whereas the impression section offers a diagnosis based on these findings.

**4.2.2 Anonymization and quality control of CT-RATE** To ensure the integrity of the radiology reports in the CT-RATE dataset, we first anonymized them by removing all personal information pertaining to patients and medical professionals. This process involved targeted searches using regular expressions to identify and eliminate date-related information and patient-doctor identifiers. Subsequently, these anonymized reports were translated from Turkish to English using the Google Translate API, and bilingual final-year medical students reviewed and corrected all translations. They also thoroughly examined each report to remove any residual personal information and ensure coherence. Only the English versions of these radiology reports were included in our CT-RATE dataset.

For the CT volumes, we implemented several quality control measures. We excluded volumes that involved contrast material or body parts other than the chest. Each chest CT volume’s orientation was standardized by examining its metadata to ensure consistency across the dataset. Additionally, we meticulously removed all identifying information about patients and medical professionals from the metadata. The remaining metadata were open-sourced as part of the CT-RATE dataset. Extended Data Table 1 provides a detailed explanation of these metadata attributes.

**4.2.3 Automatic report classification** To develop an automated label extractor model, we annotated 1,000 radiology reports by merging findings and impression sections, as some abnormalities were not explicitly mentioned in a single section. This created a multi-label dataset for each radiology report, identifying 18 distinct anomalies. Conditions not referenced in either section were considered absent. Similar conditions were grouped: left and right mucoid impactions under *mucoid impaction*, and various lung opacities (lung opacity, density increase, and ground-glass opacities) under *lung opacity*. Lung and fissural nodules were categorized as *lung nodules*. The annotated radiology reports were divided into training (80%, 800 reports) and validation (20%, 200 reports) sets. Leveraging this dataset, we fine-tuned the RadBERT-RoBERTa-4m model [25], which was originally trained on over 4 million radiology reports. Then, we applied it to classify the remaining 24,692 reports. These classified reports served three purposes: training the supervised baseline model, fine-tuning the self-supervised model, and internal evaluation. Figure 1b illustrates the automated classification process for radiology reports.

**4.2.4 Preprocessing volumes** Our preprocessing approach, inspired by previous work [19], involved several key steps to standardize all chest CT volumes in the CT-RATE dataset. First, each volume was resized to achieve uniform spacing of 0.75 mm in the x-axis and y-axis and 1.5 mm in the z-axis. The CT volumes were then either center-cropped or padded to reach a consistent resolution of  $480 \times 480 \times 240$ , ensuring comprehensive inclusion of the patient’s relevant area for the interpretation.

Subsequently, we converted each CT volume to Hounsfield Unit (HU) values using intercept and slope values from the metadata. HU values, a measure of radiodensity, were clipped to a range of -1000 to 200. This range represents the practical lower and upper limits of the HU scale [42], further standardizing the data. During training, we normalized these values to a range of -1 to 1. This normalization step makes learning more effective for the network and reduces the impact of variations in the scale of HU values.

**4.2.5 External validation dataset** For external validation, we utilized the RAD-ChestCT dataset, which includes a cohort from another country [19]. This step was crucial for evaluating CT-CLIP’s performance across varied patient distributions. The dataset comprises 3,630 CT volumes, uniformly reconstructed using a single technique. Half were conducted with Siemens CT scanners, and the other half with GE Medical scanners. The number of slices ranged from 46 to 1277, with an average of 511.6 and a mode of 472. All scans were provided at a resolution of  $512 \times 512$  px. To ensure consistent evaluation, we applied identical preprocessing methods to this external dataset as used with our CT-RATE cohort.

Since the RAD-ChestCT dataset lacks a *Mosaic attenuation* label, we excluded it from our external evaluation. Furthermore, while the RAD-ChestCT dataset includes a *Calcification* label, our dataset distinguishes between *Arterial wall calcification* and *Coronary artery wall calcification*. In assessing the model accuracies on the external evaluation set, we used the higher classification probabilities between these two labels for the *Calcification* prediction during inference.

### 4.3 Developing the CT-CLIP model

The CT-CLIP model is a novel 3D adaptation of the Contrastive Language-Image Pre-Training (CLIP) framework which was originally designed for natural image-text pairs [27] and has shown excellent performance in self-supervised classification tasks with 2D medical data [11,43]. It learns to identify similarities between text and images via contrastive learning (Fig. 1d), enabling efficient zero-shot classification.

Our model adapts CLIP to 3D CT volume and radiology text report pairs. It integrates a 3D encoder, previously used for generating CT volumes [17], as the image encoder, and CXR-Bert [41], a pre-trained model for chest X-ray reports, as the text encoder. Similar to the 2D CLIP approach, our method extracts low-dimensional latent embeddings from input volumes and corresponding sections of radiological reports.

We then compute the cosine loss, which measures the similarity between these embeddings. Training the model to align the 512-dimensional projection layers from text and CT volume embeddings with the identity matrix (as shown in Fig. 1c) allows our model to identify meaningful correlations between textual information and 3D medical images. This process enables zero-shot classification and can be further enhanced through task-specific fine-tuning for supervised classification tasks.

To highlight the impact of dataset size on model performance, we conducted an ablation study. This experiment involved training the CT-CLIP model with varying sizes of the CT-RATE dataset: 9.8% (matching the size of the RAD-ChestCT dataset, the only public chest CT dataset with multi-abnormality labels [19]), 20%, 40%, 60%, 80%, and 100%. By systematically altering the sizes of these datasets, our goal was to explore and demonstrate the significant influence of dataset scale on the effectiveness of the CT-CLIP model. Figure 4c illustrates the outcomes of this ablation study.

**4.3.1 Vision transformer** As a 3D vision transformer, we utilized a component of CT-ViT [17], a network developed to generate low-dimensional tokens from high-dimensional CT volumes and reconstruct CT volumes from these tokens. CT-ViT divides CT volumes into patches measuring  $30 \times 30 \times 15$  in the coronal, sagittal, and axial planes, ensuring uniform spacing. These patches are processed by spatial and temporal transformers to yield low-dimensional CT tokens, which are then decoded to reconstruct the CT volumes. The encoder-decoder network is pre-trained autoregressively, as detailed in GenerateCT [17]. We employed only the encoder part of this network for CT-CLIP, to generate the low-dimensional CT tokens. During the CT-CLIP model’s training phase, these encoded tokens are flattened and linearly transformed to form a 512-dimensional projection layer, resulting in the creation of encoded CT tokens. The encoding process of 3D chest CT volumes is illustrated in Fig. 1c.

**4.3.2 Text transformer** We employed the CXR-Bert text encoder, a language transformer pre-trained on chest X-ray reports [41]. This encoder can process up to 512 tokens, allowing for the comprehensive inclusion of both impression and findings sections from radiology reports. For reports with content of fewer than 512 tokens, we used padding with the <PAD> token to standardize their length.

In the CT-CLIP framework, the text encoder processes the impression and findings sections from radiology reports, converting them into a uniform format of 512 tokens. Each token is represented in 768 dimensions. These tokens are then collectively processed: summed across the 512-token span and linearly transformed. This transformation maps the tokens into a compact 512-dimensional layer, encapsulating the essential textual information from the reports. Figure 1c visually represents this encoding process. Additionally, to assess the impact of including both the impression and findings sections, we conducted an ablation study. This study involved training separate models using exclusively the impression or findings sections, allowing us to compare their contributions to the model’s performance.

## 4.4 CT-CLIP for zero-shot multi-abnormality detection

**4.4.1 Open vocabulary inference method** In our CT-CLIP model, we employ an innovative approach for zero-shot multi-abnormality detection, utilizing a specialized positive-negative softmax method. This method, inspired by recent advances in 2D chest radiography analysis [11], is particularly effective for CLIP’s normalization technique across multiple classes, a crucial feature in medical imaging where images often contain several abnormalities simultaneously. We begin by extracting the model’s preliminary output scores, known as logits, using both positive (e.g., “Consolidation.”) and negative (e.g., “Not consolidation.”) prompts. The choice of prompting method for inference is determined through prompt engineering experiments. Subsequently, we apply a softmax function to these logits to transform them into probability scores. These scores indicate the likelihood of each abnormality’s presence or absence in a CT volume. We specifically focus on the probabilities generated from positive prompts,

as they signify the actual presence of abnormalities. This approach adeptly addresses the challenges of classifying multiple labels in a single image, offering a refined strategy for normalizing output scores. Figure 1e demonstrates CT-CLIP’s inference strategy for the zero-shot multi-abnormality detection task.

**4.4.2 Prompt engineering** To enhance the CT-CLIP’s performance for zero-shot multi-abnormality detection, we experimented with various prompt engineering methods. These methods were determined based on the most commonly used sentence structures associated with abnormality labels found in radiology reports. We incorporated both positive and negative prompts, which included the following formulations serving as prompts 1 to 7, respectively:

“{Abnormality} is { $\emptyset$ /not} seen.”, “{ $\emptyset$ /No} {abnormality}.”, “There is { $\emptyset$ /no} {abnormality}.”, “Findings are { $\emptyset$ /not} compatible with {abnormality}.”, “{Abnormality} is { $\emptyset$ /not} observed.”, “{Abnormality} is { $\emptyset$ /not} present.”, “{ $\emptyset$ /Not} {abnormality}.”.

Subsequently, we determined the most effective prompt engineering approach based on accuracy scores (Fig. 4b). This approach was then also applied to fine-tune the CT-CLIP model via CT-VocabFine.

## 4.5 Fine-tuning CT-CLIP for multi-abnormality detection

To enhance the performance of the CT-CLIP model in classifying multiple abnormalities, we implemented two distinct fine-tuning approaches. The first approach, called CT-VocabFine, involves fine-tuning the model while retaining its open vocabulary capabilities. The second approach, adapted from linear probing, is called CT-LiPro. This method entails training the model with an additional classification layer.

We also conducted ablations to investigate the impact of freezing pre-trained layers within CT-CLIP during fine-tuning (Supplementary Fig. 1b). Specifically, in addition to training every layer, we fine-tuned only the projection layers of the image and text encoders in the case of CT-VocabFine. For CT-LiPro, alongside training every layer, we trained the model only for the newly added classification layer.

**4.5.1 Open vocabulary fine-tuning of CT-CLIP** The first approach, open vocabulary fine-tuning of CT-CLIP (CT-VocabFine), is a modification of WISE-FT, a robust technique for fine-tuning zero-shot models [33]. In WISE-FT, the zero-shot model generates logits (preliminary output scores) using classification labels as input text prompts. The model is then fine-tuned using binary cross-entropy (BCE) [44] to compare these logits with the actual ground truth labels. This process allows the model to learn specific classification labels while maintaining its ability to function with an open vocabulary [33].

Our CT-VocabFine method adapts this approach for the multi-label classification of images, which is essential for identifying multiple co-existing abnormalities in a single chest CT volume. We generate both positive and negative prompts for each abnormality and then concatenate their respective logits into a unified array of 36 elements (two logits for each of the 18 abnormalities).

The ground truth labels are represented as binary arrays (1s and 0s), where 1 indicates a positive logit if the ground truth is *True* and vice versa for *False*. For example, if a volume’s label is *True* for a specific abnormality, it corresponds to [1, 0] in the ground truth array; *False* would be represented as [0, 1]. The model training aligns these ground truth values with the computed logits.

To optimize computational efficiency, we divide the 36-element array into smaller segments of 12 elements for each gradient run. Figure 2c depicts the fine-tuning process in CT-VocabFine. This method retains CT-CLIP’s open vocabulary functionality, ensuring its versatility for various tasks like text-to-image retrieval. The inference strategies of both CT-CLIP and CT-VocabFine are the same (Fig. 2d).

**4.5.2 Linear probing fine-tuning of CT-CLIP** Our second fine-tuning strategy, linear probing fine-tuning of CT-CLIP (CT-LiPro), involved adapting the vision transformer of the CT-CLIP model for classification tasks. This was achieved by integrating a linear layer into the encoder network, a technique inspired by prior research [45]. The structure of CT-LiPro is demonstrated in Fig. 2a.

This modified classification model underwent training using verified ground truth labels. CT-LiPro was then assessed for its effectiveness using both internal and external evaluation datasets. While this approach offers the potential for improved classification accuracy, it is important to note that it also focuses the model more narrowly. Since CT-LiPro is based on fully supervised fine-tuning, its capabilities are primarily limited to the classes defined during this fine-tuning phase. Figure 2b visualizes the inference process of CT-LiPro, highlighting its specific application to the predetermined classes.

## 4.6 Experimental settings for multi-abnormality detection

**4.6.1 Fully supervised baseline model** In assessing our zero-shot and fine-tuned CT-CLIP models, we employed the CT-Net model as a fully supervised baseline [19]. Renowned for its performance in a similar CT dataset [19], CT-Net provided a robust comparison point. We trained the CT-Net model on our CT-RATE dataset, adapting the chest CT volumes to fit the model’s input requirements by resizing them to  $420 \times 420 \times 402$ . Consistent with our models, we focused on the abnormalities present in the CT-RATE dataset (Fig. 2d), targeting a more specific range of abnormalities compared to the 98 and 9 abnormalities explored in the original CT-Net study.

**4.6.2 Performance evaluation** For each abnormality, we determined classification thresholds by identifying the optimal point on the Receiver Operating Characteristic (ROC) curve, specifically the left-upper point. This analysis was conducted for zero-shot, fine-tuned, and fully supervised classification models alike. Additionally, we computed the Area Under the Receiver Operating Characteristic (AUROC) values for each abnormality, using these values as the primary metric to gauge the accuracy of the models.

To provide a comprehensive evaluation, we also calculated accuracy and precision scores for each identified pathology. These additional metrics offer more insights into the performance of the models. Furthermore, the F1 score was utilized as a crucial metric. This score, ranging between 0 and 1, represents the harmonic mean of precision and recall, thus encapsulating the overall effectiveness of the models:

$$F1 \text{ Score} = \frac{2 \cdot \text{Precision} \cdot \text{Recall}}{\text{Precision} + \text{Recall}}$$

To further validate the latent spaces generated by CT-CLIP for radiology reports and chest CT volumes, we conducted a t-SNE (t-distributed stochastic neighbor embedding) analysis [46]. This analysis was performed on the latent values of individual reports and CT volumes within the CT-RATE dataset, enabling us to map the positions of abnormalities visually, the distribution of abnormality groups, and other relevant attributes within the t-SNE embeddings (Extended Data Figures 1,2).

**4.6.3 Statistical analysis** For robust statistical analysis of our model evaluations, we employed the non-parametric bootstrap method to analyze the distribution of our predictions across internal and external validation sets. This process involved 500 iterations of random sampling with replacement from the original dataset. In each iteration, we selected sample sets of size  $n$ , equivalent to the number of evaluation images in the dataset, and calculated the average metric values for each bootstrap sample. To quantify the dispersion of the resulting distribution, we computed the standard deviation of these bootstrap values. For assessing statistical significance, we utilized a two-sided paired permutation test with 1,000 permutations to evaluate the observed differences in performance between the two models across AUROC, F1 score, accuracy, and precision metrics, drawing inspiration from previous work [47]. Supplementary Table 4 provides detailed comparisons between each of the two models.

## 4.7 Applying CT-CLIP for CT volume retrieval

Image retrieval involves identifying the most relevant image from a pool of candidates based on either textual [48] or visual [49] input. With CT-CLIP, trained to associate CT volumes with text reports, volume retrieval becomes feasible, complementing its zero-shot multi-abnormality classification capabilities. CT-CLIP accurately identifies the most pertinent CT volume from all available options, whether given a textual description or another volume as input. This is achieved by computing the cosine similarity among all pairs of volumes and reports, as well as among volume pairs, within a unified embedding space.

**4.7.1 Volume-to-volume retrieval** To conduct volume-to-volume retrieval, we calculated the cosine similarity between the latent embeddings of a specific chest CT volume in the validation set and all other abnormal chest CT volumes within the same set. We then ranked the chest CT volumes based on their cosine similarity scores to identify the most relevant matches for a given chest CT volume. This volume-to-volume retrieval process is illustrated in Fig. 6a.

To evaluate this retrieval task’s performance, we adapted the Mean Average Precision at  $K$  (MAP@K) metric, typically used in image-to-image retrieval tasks [34]. In this metric, an image is considered relevant if it matches the classes of the target input. Precision is then calculated as the proportion of relevant images within the top  $K$  retrieved images. Relevance is determined using the intersection over the union of the abnormality labels marked as *True* in the ground truth with those in the retrieved chest CT volume. The Average Precision at  $K$  (AP@K) is defined as follows:



$$\text{AP@K} = \frac{1}{K} \sum_{i=1}^K P_i \times R_i$$

Here,  $P_i$  is the precision at the  $i$ -th position, and  $R_i$  is the relevance at the  $i$ -th position. The final class retrieval accuracy is given by:

$$\text{MAP@K} = \frac{1}{n} \text{AP@K}$$

Where  $n$  is the total number of samples. It is important to note that as  $K$  increases, MAP@K may decrease due to the inclusion of less relevant images. We utilized the vision transformers of CT-CLIP and CT-VocabFine for volume-to-volume retrieval and assessed their performance across both internal and external validation sets using MAP@1, MAP@5, MAP@10, and MAP@50 metrics.

The Recall@K metric, which calculates the probability of the target image being within the top  $K$  retrieved images, has not been utilized in image-to-image retrieval tasks. To compute this metric, image embeddings are first generated for all images within a validation set. Subsequently, cosine similarity scores are computed between the embeddings of the query image and all images in the validation set, including the query. The top  $K$  embeddings with the highest similarities are then identified, and the likelihood of the original image being among these top  $K$  is determined. This method was not applied in image-to-image retrieval due to the inherent limitation that the cosine similarity for identical images would inevitably be the highest, resulting in a consistent Recall@K value of 1. However, this issue does not arise in text-to-image retrieval since the query is based on text embeddings rather than image embeddings.

**4.7.2 Report-to-volume retrieval** For report-to-volume retrieval, we utilized our models to generate vector embeddings for both radiology reports and CT volumes. Our goal was to find the CT volume that best matched each query report. To achieve this, we computed the cosine similarity between the latent representations of each report and all the CT volumes, achieved by calculating the dot product of unit vectors. Subsequently, we ranked the CT volumes based on their cosine similarity scores to identify and return the most relevant matches. The process of report-to-volume retrieval is depicted in Figure 6b.

For the evaluation of this task, we employed the Recall@K metric, where  $K$  represents the number of returned images. This method serves as a standard evaluation tool in text-to-image retrieval tasks [35]. We assessed four Recall@K metrics: Recall@5, Recall@10, Recall@50, and Recall@100. These metrics measure the frequency of the target image appearing among the top 5, 10, 50, and 100 retrieved images, respectively. It is worth noting that the external validation set lacked text reports. Therefore, we restricted the report-to-volume retrieval evaluation to the internal validation set. We assessed both the CT-CLIP and CT-VocabFine models for this task. However, since the supervised model and CT-LiPro do not generate latent embeddings for reports, they were not utilized in the report-to-volume retrieval.

## 4.8 Computational hardware and software

The experiments were executed using Python version 3.11.5. Our software environment comprised PyTorch v.2.0.1, CUDA v.11.7, scipy v.1.11.1, torchvision v.0.15.2, scikit-learn v.1.3.0, scikit-image v.0.20.0, pandas v.2.0.3, numpy v.1.24.4, transformers v4.30.1, and accelerate v0.21.1. Comprehensive details on our software packages and computational environment are accessible on our GitHub repository. For computational resources, we deployed four 80GB A100 GPUs, with 500GB of RAM and 24 CPUs, primarily for CT-CLIP training. The training of CT-CLIP employed the Distributed Data-Parallel approach using the Accelerate library, incorporating the Fully Sharded Data Parallelism technique for efficient multi-GPU training. In contrast, fine-tuning of CT-CLIP, training of the fully supervised classification model, and other experiments were conducted on a single A100 GPU. Detailed information about the hyperparameters utilized during the training of all models is provided in Supplementary Table 3.

## Data availability

Our CT-RATE dataset, comprising paired chest CT volumes and radiology text reports, is publicly accessible via <https://huggingface.co/datasets/ibrahimhamamci/CT-RATE>. Additionally, the external validation set, RAD-ChestCT, is openly accessible through <https://zenodo.org/records/6406114>.

## Code availability

Our trained models and associated source code are publicly available for further research and development at <https://github.com/ibrahimthemhamamci/CT-CLIP>.

## Author contributions

I.E.H., S.E., and B.M. designed the study. I.E.H. and S.E. were responsible for data collection, data analysis, model construction, model validation, figure preparation, and manuscript writing. F.A., A.G.S., S.N.E., and I.D. managed data anonymization and annotation. M.F.D. contributed model construction and manuscript writing. B.W., E.S., M.S., E.B.E., A.A., A.S., B.L., and M.K.O. provided knowledge support. B.M. supervised the study. All authors reviewed the manuscript and approved the final version.

## Acknowledgments

We extend our gratitude to the Helmut Horten Foundation for their invaluable support to our research. Additionally, we would like to express our sincere appreciation to Istanbul Medipol University Mega Hospital for their support and provision of data. Figures 1, 2, and 6 were created with *BioRender.com*.

## References

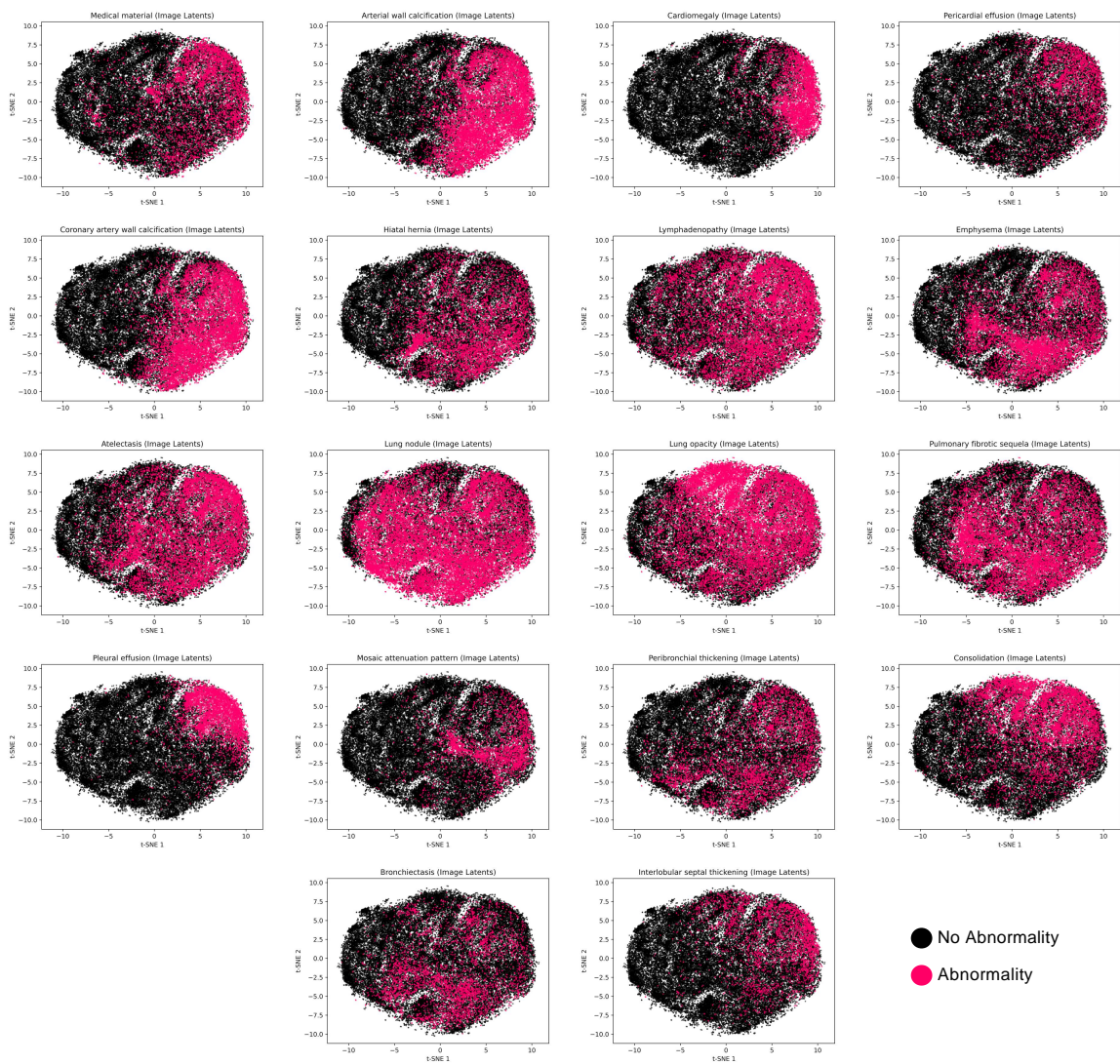
1. A. Esteva, K. Chou, S. Yeung, N. V. Naik, A. Madani, A. Mottaghi, Y. Liu, E. J. Topol, J. Dean, and R. Socher, "Deep learning-enabled medical computer vision," *NPJ Digital Medicine*, vol. 4, 2021.
2. C. Qin, D. Yao, Y. Shi, and Z. Song, "Computer-aided detection in chest radiography based on artificial intelligence: a survey," *BioMedical Engineering OnLine*, vol. 17, 2018.
3. J. Lipková, T. Y. Chen, M. Y. Lu, R. J. Chen, M. Shady, M. Williams, J. Wang, Z. Noor, R. N. Mitchell, M. Turan, G. Coskun, F. Yilmaz, D. Demir, D. Nart, K. Başak, N. Turhan, S. Ozkara, Y. Banz, K. E. Odening, and F. Mahmood, "Deep learning-enabled assessment of cardiac allograft rejection from endomyocardial biopsies," *Nature Medicine*, vol. 28, pp. 575 – 582, 2022.
4. I. E. Hamamci, S. Er, E. Simsar, A. K. Sekuboyina, M. Gundogar, B. Stadlinger, A. C. Mehl, and B. H. Menze, "Diffusion-based hierarchical multi-label object detection to analyze panoramic dental x-rays," in *International Conference on Medical Image Computing and Computer-Assisted Intervention*, 2023.
5. S. Pati, S. P. Thakur, M. M. Bhalerao, U. Baid, C. M. Grenko, B. Edwards, M. J. Sheller, J. L. Agraz, B. Baheti, V. Bashyam, P. Sharma, B. Haghighi, A. Gastounioti, M. Bergman, B. H. Menze, D. Kontos, C. Davatzikos, and S. Bakas, "Gandlf: the generally nuanced deep learning framework for scalable end-to-end clinical workflows," *Communications Engineering*, vol. 2, no. 1, p. 23, 2023.
6. A. E. W. Johnson, T. J. Pollard, S. J. Berkowitz, N. R. Greenbaum, M. P. Lungren, C. ying Deng, R. G. Mark, and S. Horng, "Mimic-cxr, a de-identified publicly available database of chest radiographs with free-text reports," *Scientific Data*, vol. 6, 2019.
7. X. Wang, Y. Peng, L. Lu, Z. Lu, M. Bagheri, and R. M. Summers, "Chestx-ray8: Hospital-scale chest x-ray database and benchmarks on weakly-supervised classification and localization of common thorax diseases," in *2017 IEEE Conference on Computer Vision and Pattern Recognition (CVPR)*, pp. 3462–3471, 2017.
8. H. Q. Nguyen, K. Lam, L. T. Le, H. Pham, D. Q. Tran, D. B. Nguyen, D. D. Le, C. M. Pham, H. Tong, D. H. Dinh, C. D. Do, L. T. Doan, C. N. Nguyen, B. T. Nguyen, Q. V. Nguyen, A. D. Hoang, H. N. Phan, A. T. Nguyen, P. Ho, D. T. Ngo, N. T. Nguyen, N. T. Nguyen, M.-S. Dao, and V. Vu, "Vindr-cxr: An open dataset of chest x-rays with radiologist's annotations," *Scientific Data*, vol. 9, 2020.
9. J. A. Irvin, P. Rajpurkar, M. Ko, Y. Yu, S. Ciurea-Ilcus, C. Chute, H. Marklund, B. Haghoo, R. L. Ball, K. S. Shpanskaya, J. Seekins, D. A. Mong, S. S. Halabi, J. K. Sandberg, R. Jones, D. B. Larson, C. Langlotz, B. N. Patel, M. P. Lungren, and A. Ng, "Chexpert: A large chest radiograph dataset with uncertainty labels and expert comparison," in *AAAI Conference on Artificial Intelligence*, 2019.
10. I. E. Hamamci, S. Er, E. Simsar, A. E. Yuksel, S. Gultekin, S. Ozdemir, K. Yang, H. Li, S. Pati, B. Stadlinger, A. C. Mehl, M. Gundogar, and B. H. Menze, "Dentex: An abnormal tooth detection with dental enumeration and diagnosis benchmark for panoramic x-rays," *ArXiv*, vol. abs/2305.19112, 2023.
11. E. Tiu, E. Talius, P. Patel, C. P. Langlotz, A. Y. Ng, and P. Rajpurkar, "Expert-level detection of pathologies from unannotated chest x-ray images via self-supervised learning," *Nature Biomedical Engineering*, vol. 6, pp. 1399 – 1406, 2022.
12. M. Y. Lu, B. Chen, D. F. K. Williamson, R. J. Chen, I. Liang, T. Ding, G. Jaume, I. Odintsov, L. P. Le, G. Gerber, A. V. Parwani, A. Zhang, and F. Mahmood, "A visual-language foundation model for computational pathology," *Nature Medicine*, 2024.
13. X. Chen, X. Wang, K. Zhang, R. Zhang, K.-M. Fung, T. C. Thai, K. M. Moore, R. S. Mannel, H. Liu, B. Zheng, and Y. Qiu, "Recent advances and clinical applications of deep learning in medical image analysis," *Medical Image Analysis*, vol. 79, p. 102444, 2021.
14. S. P. Singh, L. Wang, S. Gupta, H. Goli, P. Padmanabhan, and B. Guly'as, "3d deep learning on medical images: a review," *Sensors (Basel, Switzerland)*, vol. 20, 2020.
15. S. K. Zhou, H. Greenspan, C. Davatzikos, J. S. Duncan, B. van Ginneken, A. Madabhushi, J. L. Prince, D. Rueckert, and R. M. Summers, "A review of deep learning in medical imaging: Imaging traits, technology trends, case studies with progress highlights, and future promises," *Proceedings of the IEEE*, vol. 109, pp. 820–838, 2020.

16. M. J. Willeminck, W. A. Koszek, C. Hardell, J. Wu, D. Fleischmann, H. Harvey, L. R. Folio, R. M. Summers, D. Rubin, and M. P. Lungren, "Preparing medical imaging data for machine learning," *Radiology*, p. 192224, 2020.
17. I. E. Hamamci, S. Er, E. Simsar, A. Tezcan, A. Simsek, F. Almas, S. N. Esirgun, H. Reynaud, S. Pati, C. Blüthgen, and B. H. Menze, "Generatect: Text-guided 3d chest ct generation," *ArXiv*, vol. abs/2305.16037, 2023.
18. J. Gao, T. Shen, Z. Wang, W. Chen, K. Yin, D. Li, O. Litany, Z. Gojcic, and S. Fidler, "Get3d: A generative model of high quality 3d textured shapes learned from images," *ArXiv*, vol. abs/2209.11163, 2022.
19. R. L. Draelos, D. Dov, M. A. Mazurowski, J. Y. Lo, R. Henao, G. D. Rubin, and L. Carin, "Machine-learning-based multiple abnormality prediction with large-scale chest computed tomography volumes," *Medical Image Analysis*, vol. 67, p. 101857, 2020.
20. T. Chen, S. Kornblith, M. Norouzi, and G. E. Hinton, "A simple framework for contrastive learning of visual representations," in *ArXiv*, vol. abs/2002.05709, 2020.
21. Y. Xian, B. Schiele, and Z. Akata, "Zero-shot learning-the good, the bad and the ugly," in *2017 IEEE Conference on Computer Vision and Pattern Recognition (CVPR)*, pp. 3077–3086, 2017.
22. Y. Zhang, H. Jiang, Y. Miura, C. D. Manning, and C. Langlotz, "Contrastive learning of medical visual representations from paired images and text," in *Machine Learning in Health Care*, 2020.
23. M. J. Willeminck and P. B. Noël, "The evolution of image reconstruction for ct—from filtered back projection to artificial intelligence," *European Radiology*, vol. 29, pp. 2185 – 2195, 2018.
24. C. Sager, C. Janiesch, and P. Zschech, "A survey of image labelling for computer vision applications," *Journal of Business Analytics*, vol. 4, pp. 91 – 110, 2021.
25. A. Yan, J. McAuley, X. Lu, J. Du, E. Y. Chang, A. Gentili, and C.-N. Hsu, "Radbert: Adapting transformer-based language models to radiology," *Radiology. Artificial intelligence*, vol. 4 4, p. e210258, 2022.
26. S. Minaee, E. Cambria, and J. Gao, "Deep learning-based text classification: A comprehensive review," *ACM Computing Surveys*, vol. 54, pp. 1 – 40, 2020.
27. A. Radford, J. W. Kim, C. Hallacy, A. Ramesh, G. Goh, S. Agarwal, G. Sastry, A. Askell, P. Mishkin, J. Clark, G. Krueger, and I. Sutskever, "Learning transferable visual models from natural language supervision," in *International Conference on Machine Learning*, 2021.
28. H. Zhang, J. Y. Koh, J. Baldridge, H. Lee, and Y. Yang, "Cross-modal contrastive learning for text-to-image generation," in *2021 IEEE/CVF Conference on Computer Vision and Pattern Recognition (CVPR)*, pp. 833–842, 2021.
29. A. Aljuaid and M. Anwar, "Survey of supervised learning for medical image processing," *Sn Computer Science*, vol. 3, 2022.
30. G. Yong, K. Jeon, D. Gil, and G. Lee, "Prompt engineering for zero-shot and few-shot defect detection and classification using a visual-language pretrained model," *Computer-Aided Civil and Infrastructure Engineering*, vol. 38, pp. 1536 – 1554, 2022.
31. A. Bailly, C. Blanc, É. Francis, T. Guillotin, F. Jamal, B. Wakim, and P. Roy, "Effects of dataset size and interactions on the prediction performance of logistic regression and deep learning models," *Computer Methods and Programs in Biomedicine*, vol. 213, p. 106504, 2022.
32. X. Zhai, A. Kolesnikov, N. Houlsby, and L. Beyer, "Scaling vision transformers," in *2022 IEEE/CVF Conference on Computer Vision and Pattern Recognition (CVPR)*, pp. 1204–1213, 2021.
33. M. Wortsman, G. Ilharco, M. Li, J. W. Kim, H. Hajishirzi, A. Farhadi, H. Namkoong, and L. Schmidt, "Robust fine-tuning of zero-shot models," in *2022 IEEE/CVF Conference on Computer Vision and Pattern Recognition (CVPR)*, pp. 7949–7961, 2021.
34. C. Chen, M. Y. Lu, D. F. K. Williamson, T. Y. Chen, A. J. Schaumberg, and F. Mahmood, "Fast and scalable search of whole-slide images via self-supervised deep learning," *Nature Biomedical Engineering*, vol. 6, pp. 1420 – 1434, 2022.
35. S. Zhang, M. Yang, T. Cour, K. Yu, and D. N. Metaxas, "Query specific fusion for image retrieval," in *European Conference on Computer Vision*, 2012.
36. J. Li, G. Zhu, C. Hua, M. Feng, B. Bennamoun, P. Li, X. Lu, J. Song, P. Shen, X. Xu, L. Mei, L. Zhang, S. A. A. Shah, and Bennamoun, "A systematic collection of medical image datasets for deep learning," *ACM Computing Surveys*, 2021.
37. A. Ioannidou, E. Chatzilari, S. Nikolopoulos, and I. Kompatsiaris, "Deep learning advances in computer vision with 3d data: A survey," *ACM Computing Surveys*, vol. 50, pp. 1 – 38, 2017.
38. S. Wang, C. Li, R. Wang, Z. Liu, M. Wang, H. Tan, Y. Wu, X. Liu, H. Sun, R. Yang, X. Liu, J. Chen, H.-C. Zhou, I. B. Ayed, and H. Zheng, "Annotation-efficient deep learning for automatic medical image segmentation," *Nature Communications*, vol. 12, 2020.
39. M. P. Hartung, I. C. Bickle, F. Gaillard, and J. P. Kanne, "How to create a great radiology report," *RadioGraphics*, vol. 40, no. 6, pp. 1658–1670, 2020.
40. C. J. Kelly, A. Karthikesalingam, M. Suleyman, G. C. Corrado, and D. King, "Key challenges for delivering clinical impact with artificial intelligence," *BMC Medicine*, vol. 17, 2019.
41. B. Boecking, N. Usuyama, S. Bannur, D. C. de Castro, A. Schwaighofer, S. L. Hyland, M. T. Wetscherek, T. Naumann, A. Nori, J. Alvarez-Valle, H. Poon, and O. Oktay, "Making the most of text semantics to improve biomedical vision-language processing," in *European Conference on Computer Vision*, 2022.

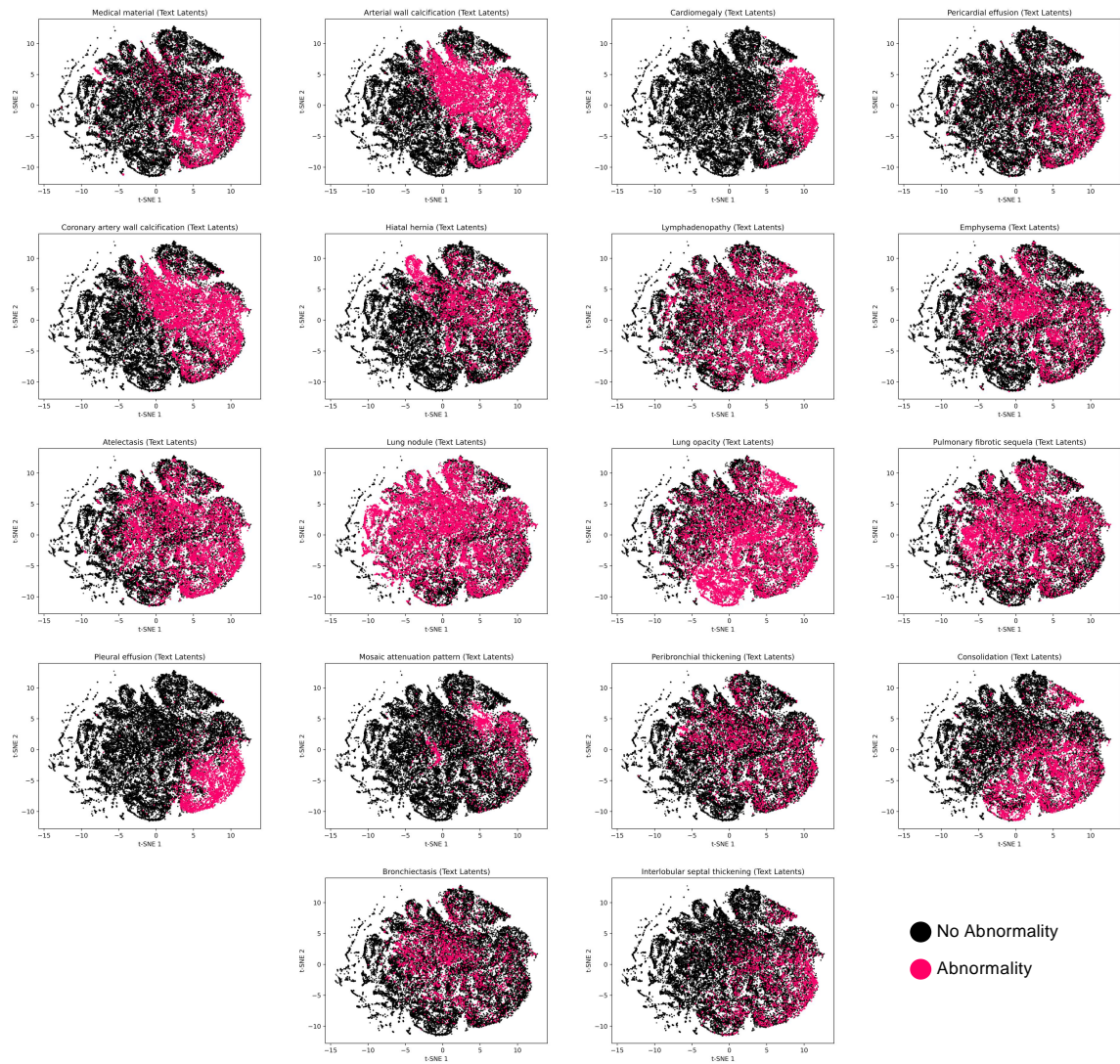
42. T. D. DenOtter and J. Schubert, "Hounsfield unit," 2019.
43. Z. Huang, F. Bianchi, M. Yuksekogonul, T. J. Montine, and J. Y. Zou, "A visual–language foundation model for pathology image analysis using medical twitter," *Nature Medicine*, vol. 29, pp. 2307–2316, 2023.
44. Z. Zhang and M. R. Sabuncu, "Generalized cross entropy loss for training deep neural networks with noisy labels," *ArXiv*, vol. abs/1805.07836, 2018.
45. G. Alain and Y. Bengio, "Understanding intermediate layers using linear classifier probes," *ArXiv*, vol. abs/1610.01644, 2016.
46. L. van der Maaten and G. E. Hinton, "Visualizing data using t-sne," *Journal of Machine Learning Research*, vol. 9, pp. 2579–2605, 2008.
47. R. J. Chen, T. Ding, M. Y. Lu, D. F. K. Williamson, G. Jaume, A. H. Song, B. Chen, A. Zhang, D. Shao, M. Shaban, M. Williams, L. Oldenburg, L. L. Weishaupt, J. J. Wang, A. Vaidya, L. P. Le, G. Gerber, S. Sahai, W. Williams, and F. Mahmood, "Towards a general-purpose foundation model for computational pathology.," *Nature Medicine*, 2024.
48. M. L. Kherfi, D. Ziou, and A. Bernardi, "Image retrieval from the world wide web: Issues, techniques, and systems," *ACM Computing Surveys*, vol. 36, pp. 35–67, 2004.
49. N. Hegde, J. D. Hipp, Y. Liu, M. R. Emmert-Buck, E. Reif, D. Smilkov, M. Terry, C. J. Cai, M. B. Amin, C. H. Mermel, P. Q. Nelson, L. H. Peng, G. S. Corrado, and M. C. Stumpe, "Similar image search for histopathology: Smily," *NPJ Digital Medicine*, vol. 2, 2019.

Attribute	Explanation
VolumeName	The file name.
Manufacturer	Manufacturer of the equipment that produced the Composite Instances.
SeriesDescription	Description of the Series.
ManufacturerModelName	Manufacturer's model name of the equipment that is to be used for beam delivery.
PatientSex	Sex of the named Patient.
PatientAge	Age of the Patient.
ReconstructionDiameter	Diameter, in mm, of the region from within which the data was used in creating the reconstruction of the image. Data may exist outside this region and portions of the patient may exist outside this region.
DistanceSourceToDetector	Distance in mm from source to detector center.
DistanceSourceToPatient	Distance in mm from source to the table, support or bucky side that is closest to the Imaging Subject, as measured along the central ray of the X-Ray beam.
GantryDetectorTilt	Nominal angle of tilt in degrees of the scanning gantry. Not intended for mathematical computations.
TableHeight	The height of the patient table in mm. The range and values of this element are determined by the manufacturer.
RotationDirection	Direction of rotation of the source when relevant, about nearest principal axis of equipment.
ExposureTime	Duration of X-Ray exposure in msec.
XRayTubeCurrent	X-Ray Tube Current in mA.
Exposure	The exposure expressed in mAs, for example calculated from Exposure Time and X-Ray Tube Current.
FilterType	Type of filter(s) inserted into the X-Ray beam (e.g., wedges).
GeneratorPower	Power in kW to the X-Ray generator.
FocalSpots	Nominal focal spot size in mm used to acquire this image.
ConvolutionKernel	A label describing the convolution kernel or algorithm used to reconstruct the data. A single value shall be present.
PatientPosition	Patient position descriptor relative to the equipment.
RevolutionTime	The time in seconds of a complete revolution of the source around the gantry orbit.
SingleCollimationWidth	Adjacent physical detector rows may have been combined to form a single effective acquisition row.
TotalCollimationWidth	This will be equal the number of effective detector rows multiplied by single collimation width.
TableSpeed	The distance in mm that the table moves in one second during the gathering of data that resulted in this image.
TableFeedPerRotation	Motion of the table (in mm) during a complete revolution of the source around the gantry orbit.
SpiralPitchFactor	Ratio of the Table Feed per Rotation to the Total Collimation Width.
DataCollectionCenterPatient	The x, y, and z coordinates (in the Patient-Based Coordinate System) in mm of the center of the region in which data were collected.
ReconstructionTargetCenterPatient	If the reconstructed image is not magnified or panned the value corresponds with the Data Collection Center Attribute.
ExposureModulationType	A multi-valued label describing the type of current modulation used for the purpose of limiting the dose.
CTDIvol	It describes the average dose for this image for the selected CT conditions of operation.
ImagePositionPatient	Image Position specifies the x, y, and z coordinates of the upper left hand corner of the image; it is the center of the first voxel transmitted.
ImageOrientationPatient	Image Orientation specifies the direction cosines of the first row and the first column with respect to the patient.
SliceLocation	Slice Location is defined as the relative position of the image plane expressed in mm. This information is relative to an unspecified implementation specific reference point.
SamplesPerPixel	Samples per Pixel is the number of separate planes in this image.
PhotometricInterpretation	The value of Photometric Interpretation specifies the intended interpretation of the image pixel data.
Rows	Number of rows in the image.
Columns	Number of columns in the image.
XYSpacing	Physical distance between the center of each pixel along the x and y axes, respectively, in the patient.
RescaleIntercept	The value b in relationship between stored values (SV) and the output units.
RescaleSlope	m in the equation specified by Rescale Intercept.
RescaleType	Specifies the output units of Rescale Slope and Rescale Intercept.
NumberOfSlices	Number of slices.
ZSpacing	Physical distance between the center of each pixel along the z axis in the patient.
StudyDate	Date the Study started.

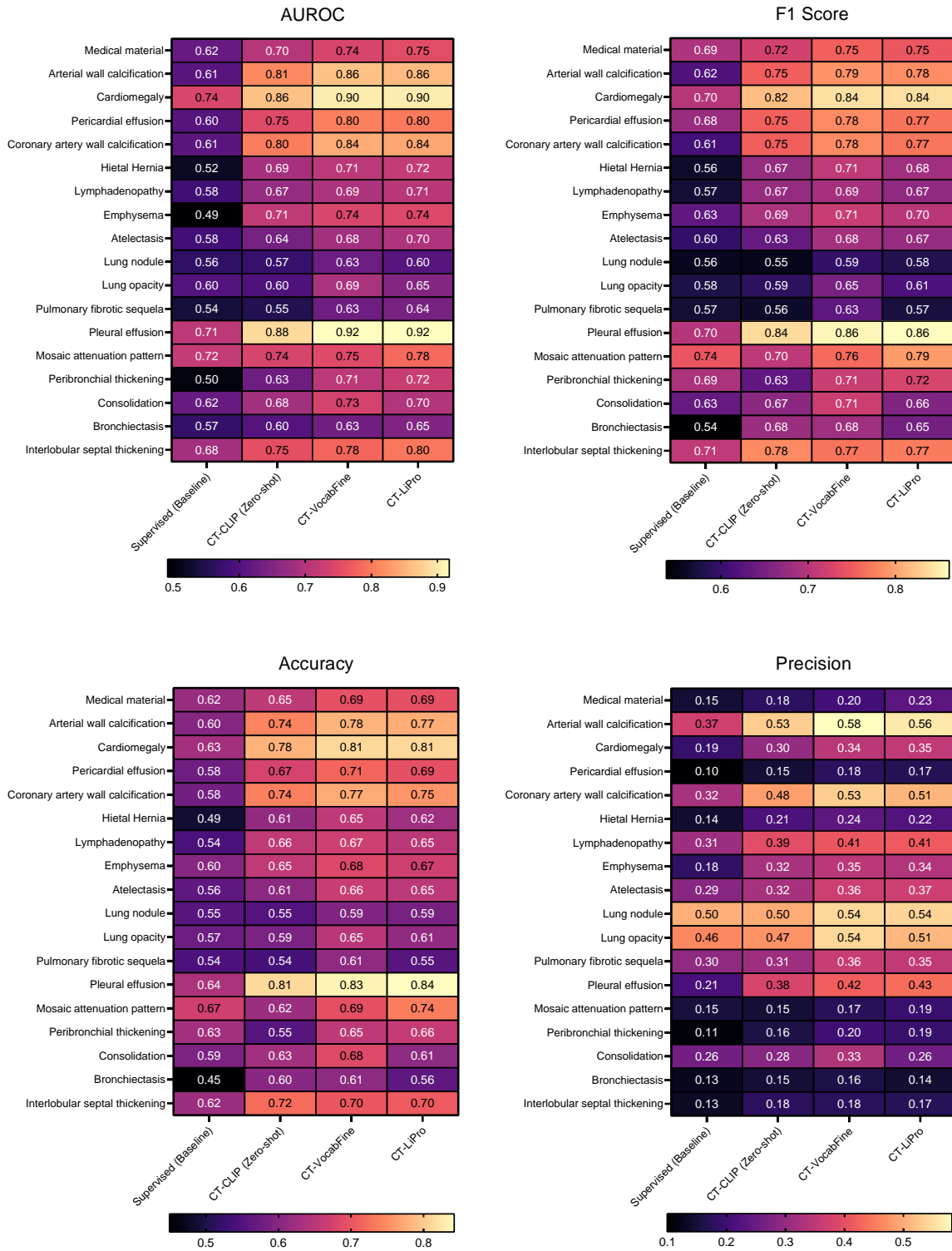
**Extended Data Table 1: Metadata attributes.** Detailed breakdown of the metadata attributes accessible within the CT-RATE dataset, providing a thorough understanding of the dataset's composition.



Extended Data Figure 1: Abnormality-based t-SNE plots for chest CT volumes.

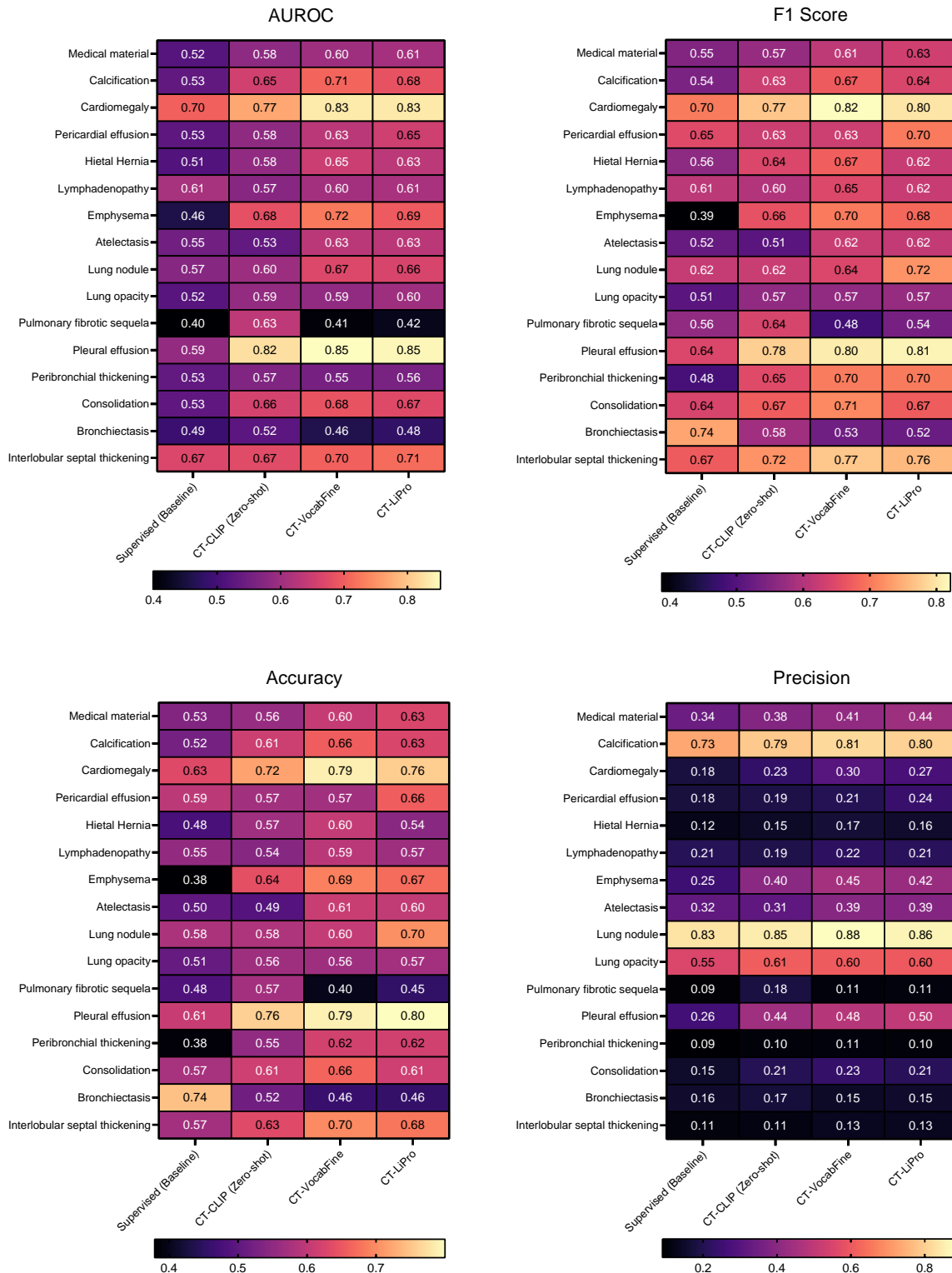


Extended Data Figure 2: Abnormality-based t-SNE plots for radiology text reports.



**Extended Data Figure 3: Comparison of abnormality-based performance metrics in the internal validation set.** This figure provides a detailed analysis of performance metrics, including AUROC, accuracy, precision, and F1 scores, for detecting various abnormalities with our models in the internal validation set, compared to the fully supervised baseline model. The proposed CT-CLIP based models demonstrate improvement over the baseline in almost all comparisons.





**Extended Data Figure 4: Comparison of abnormality-based performance metrics in the external validation set.** This figure illustrates the evaluation of critical performance metrics—AUROC, accuracy, precision, and F1 scores—for our models in identifying various abnormalities within the external validation set. It highlights the models’ remarkable adaptability and superior effectiveness with distribution shifts, setting a new standard in performance compared to a fully supervised baseline model.

<b>a</b>	Abnormality	Count in train set	Count in internal validation set	Train set ratio	Internal validation set ratio
	Medical material	2387	130	0.102	0.083
	Arterial wall calcification	7136	459	0.303	0.296
	Cardiomegaly	2604	161	0.114	0.102
	Pericardial effusion	718	41	0.030	0.027
	Coronary artery wall calcification	6050	388	0.258	0.250
	Hiatal hernia	3418	220	0.143	0.139
	Lymphadenopathy	5769	385	0.245	0.250
	Emphysema	4651	304	0.192	0.197
	Atelectasis	6027	363	0.254	0.234
	Lung nodule	10892	706	0.450	0.450
	Lung opacity	8976	622	0.375	0.398
	Pulmonary fibrotic sequela	5809	380	0.240	0.240
	Pleural effusion	2967	197	0.126	0.128
	Mosaic attenuation pattern	1253	88	0.054	0.057
	Peribronchial thickening	1622	109	0.068	0.072
	Consolidation	3274	230	0.136	0.145
	Bronchiectasis	2028	147	0.084	0.093
	Interlobular septal thickening	1674	110	0.070	0.071

<b>b</b>	Manufacturer	Count in train set	Count in internal validation set	Train set ratio	Internal validation set ratio
	Philips	28966	1928	0.614	0.634
	Siemens	15946	971	0.338	0.320
	PNMS	2237	140	0.048	0.046

<b>c</b>	Sex	Count in train set	Count in internal validation set	Train set ratio	Internal validation set ratio
	Male	27462	1776	0.583	0.584
	Female	19681	1263	0.417	0.416

**Supplementary Table 1: Detailed overview of the CT-RATE dataset.** **a.** Enumerates the counts and proportions of various abnormalities identified within the training and validation subsets, offering insights into dataset composition. **b.** Details the distribution of chest CT volumes according to manufacturer across both subsets, reflecting the dataset's diversity. **c.** Illustrates the breakdown of chest CT volumes by sex in both subsets, providing a demographic perspective of the data.

Abnormality	Precision	Recall	F1 Score
Medical material	1.00	0.94	0.97
Arterial wall calcification	0.96	0.97	0.96
Cardiomegaly	1.00	0.96	0.98
Pericardial effusion	1.00	1.00	1.00
Coronary artery wall calcification	0.96	1.00	0.98
Hiatal hernia	0.96	0.96	0.96
Lymphadenopathy	0.94	1.00	0.97
Emphysema	1.00	0.96	0.98
Atelectasis	0.98	0.96	0.97
Lung nodule	0.95	1.00	0.98
Lung opacity	0.94	0.96	0.95
Pulmonary fibrotic sequela	0.97	0.96	0.96
Pleural effusion	1.00	1.00	1.00
Mosaic attenuation pattern	1.00	0.96	0.98
Peribronchial thickening	1.00	1.00	1.00
Consolidation	0.95	1.00	0.97
Bronchiectasis	1.00	0.91	0.95
Interlobular septal thickening	1.00	1.00	1.00

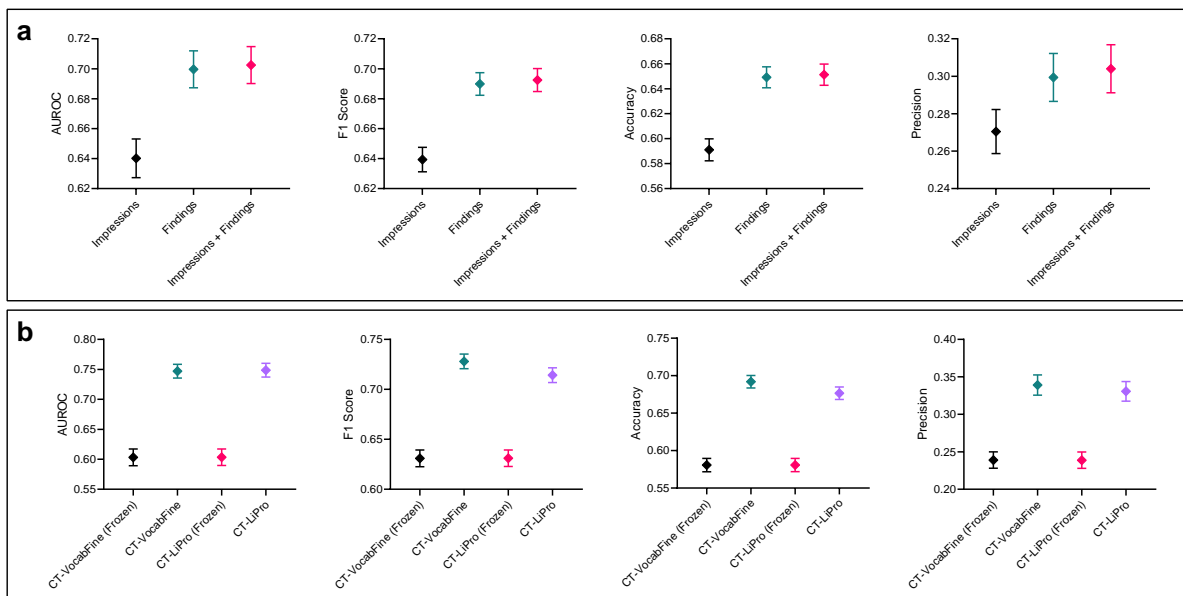
**Supplementary Table 2: Fine-tuned text encoder’s performance in automatic label extraction.** This table presents a comprehensive assessment of performance metrics—including precision, recall, and F1 scores—for the fine-tuned text encoder across various abnormalities. The evaluation underscores the encoder’s accuracy and efficiency in automating the extraction of labels for each abnormality.

	Supervised (Baseline)	CT-CLIP (Zero-shot)	CT-VocabFine	CT-LiPro
Optimizer	Adam	Adam	Adam	Adam
$\beta 1$	0.9	0.9	0.9	0.9
$\beta 2$	0.99	0.99	0.99	0.99
Learning Rate	0.001	0.00000125	0.00001	0.00001
Batch Size	4	8	1	1
Scheduler	N/A	N/A	Cosine Annealing	Cosine Annealing
Warmup Steps	N/A	N/A	10,000	10,000
Max Steps	N/A	N/A	20,000	20,000
GPUs Utilized	1	4	1	1
Train Duration	4 days	3 days	2 days	2 days
Iterations	100,000	30,000	20,000	20,000

**Supplementary Table 3: Hyperparameters for the training of each model.**

Comparison	AUROC	F1 Score	Accuracy	Precision
Supervised (Baseline) vs CT-CLIP (Zero-shot)	0.001	0.017	0.005	0.130
Supervised (Baseline) vs CT-VocabFine	<0.0001	<0.0001	<0.0001	0.030
Supervised (Baseline) vs CT-LiPro	<0.0001	0.004	<0.0001	0.047
CT-CLIP (Zero-shot) vs CT-VocabFine	0.163	0.169	0.107	0.456
CT-CLIP (Zero-shot) vs CT-LiPro	0.148	0.444	0.346	0.570
CT-VocabFine vs CT-LiPro	0.947	0.601	0.547	0.864

**Supplementary Table 4: Statistical significance of model comparisons.** Utilizing a two-sided paired permutation test with 1,000 permutations, we observe statistically significant differences ( $p < 0.05$ ) in AUROC, F1 score, and accuracy between the supervised (baseline) model and each of CT-CLIP (zero-shot), CT-VocabFine, and CT-LiPro. For precision, significant differences are noted between the supervised (baseline) model and both CT-VocabFine and CT-LiPro.



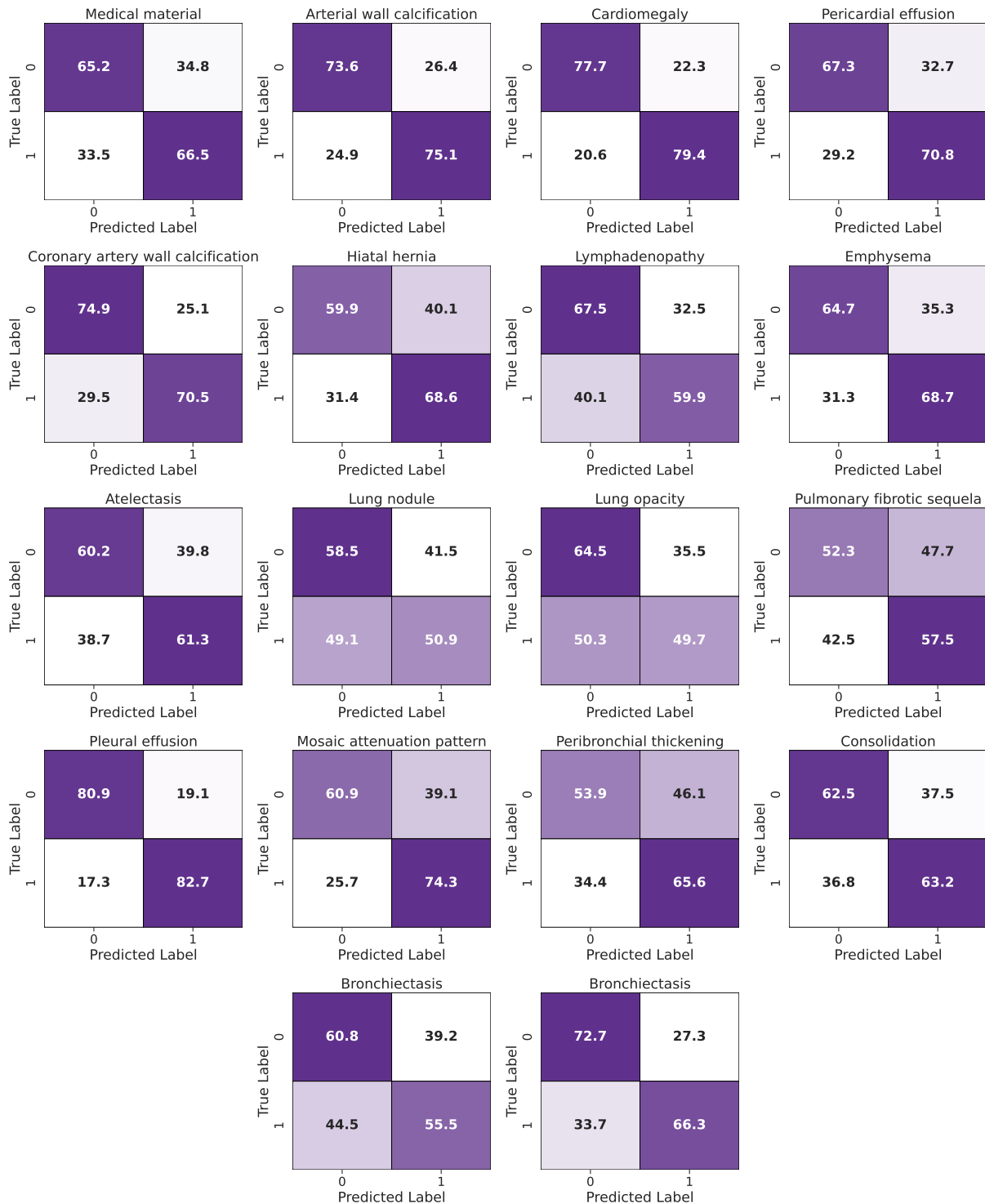
**Supplementary Figure 1: Detailed ablation study. a.** Compares the zero-shot abnormality detection performance of CT-CLIP models, each utilizing different sections of radiology text reports during training. **b.** Compares various fine-tuning techniques applied to CT-CLIP models: *frozen* models involve fine-tuning only the latent layers for the CT-Vocabfine approach, while for the CT-LiPro method, only the new linear layer is fine-tuned, leaving all other layers unchanged.

## Confusion Matrices (Supervised)



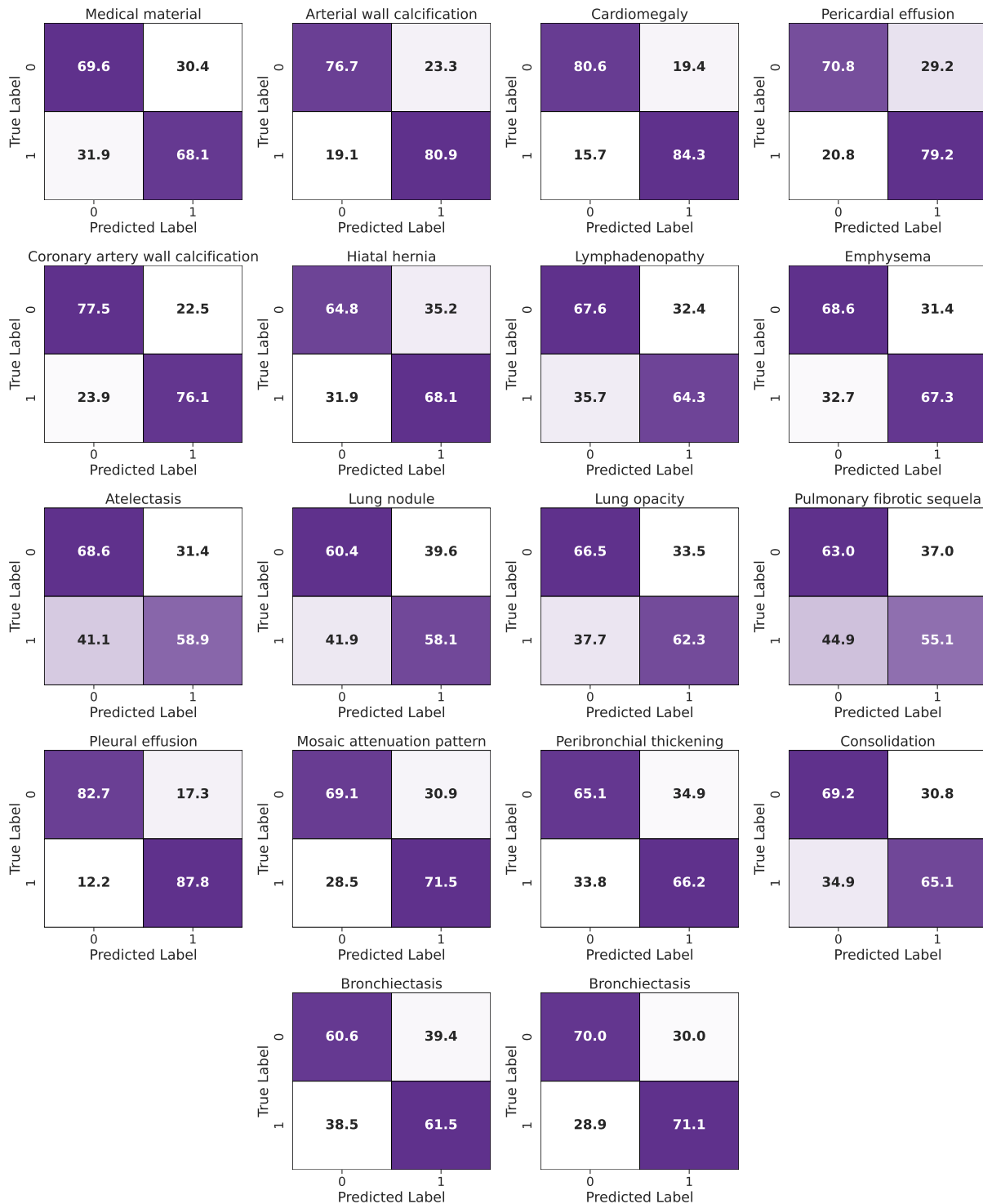
Supplementary Figure 2: Illustration of confusion matrices for the fully supervised baseline model in the internal validation set.

Confusion Matrices (CT-CLIP)



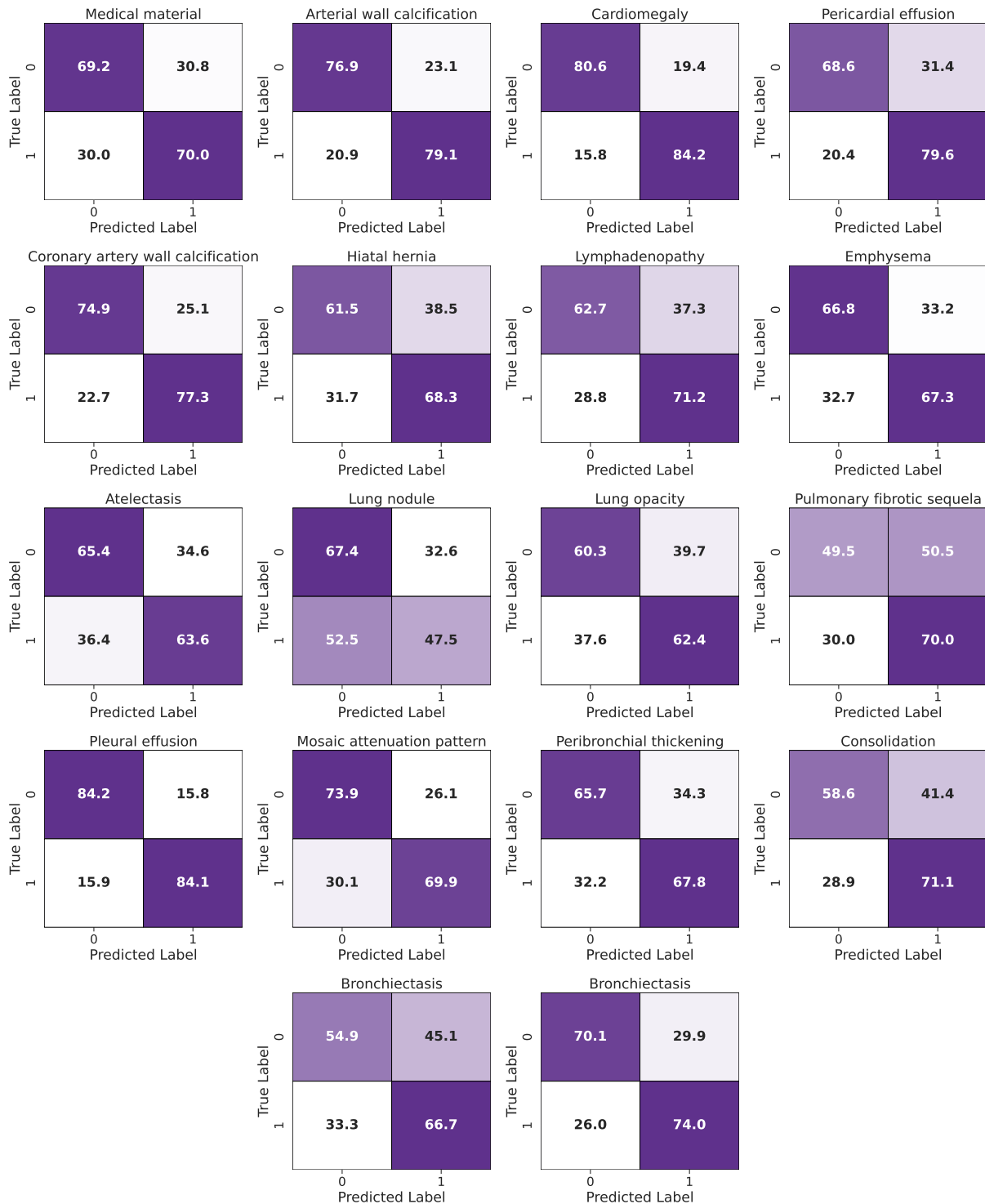
Supplementary Figure 3: Illustration of confusion matrices for the zero-shot CT-CLIP model in the internal validation set.

## Confusion Matrices (CT-VocabFine)



**Supplementary Figure 4: Illustration of confusion matrices for the fine-tuned CT-VocabFine model in the internal validation set.**

Confusion Matrices (CT-LiPro)

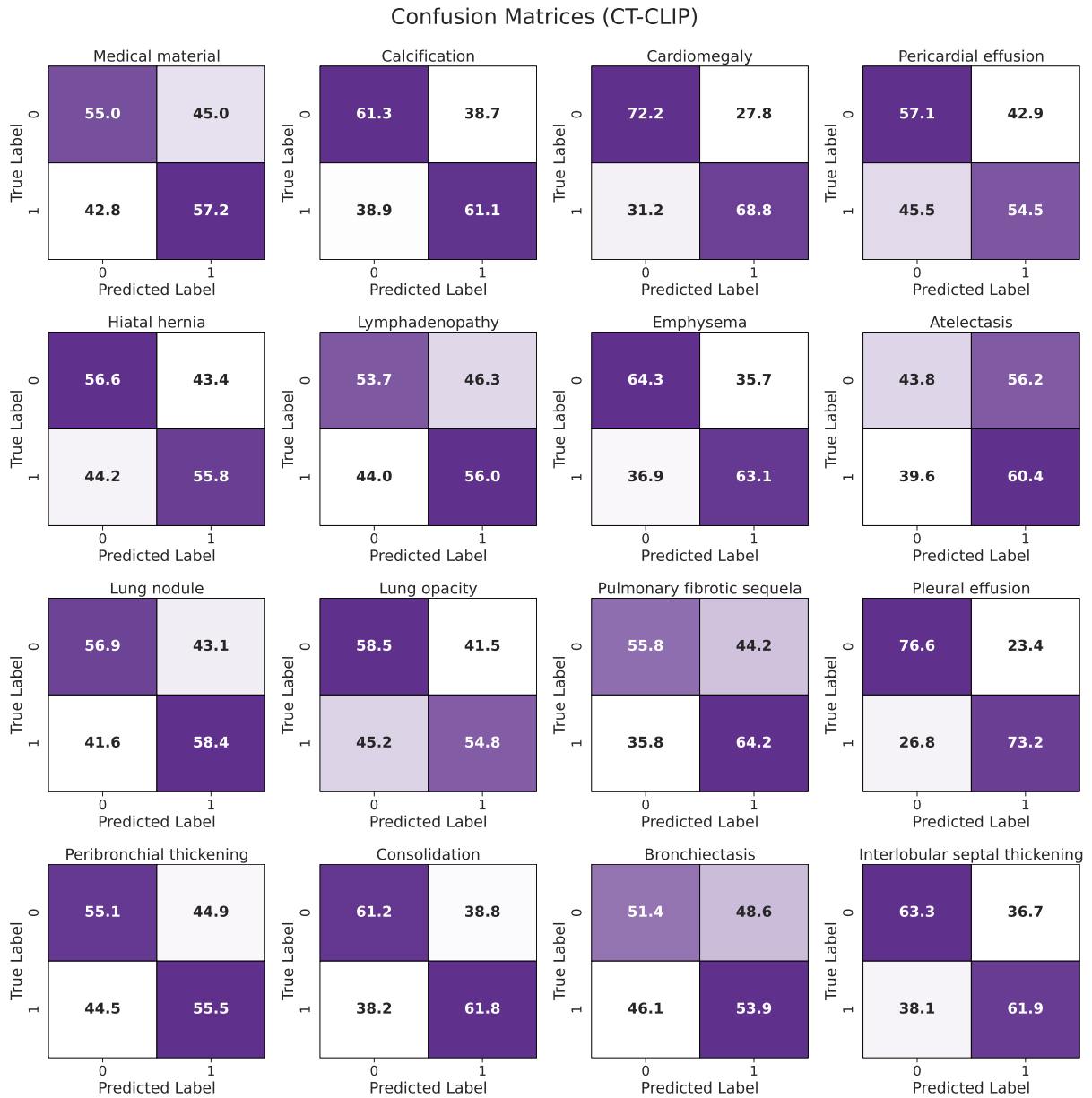


Supplementary Figure 5: Illustration of confusion matrices for the fine-tuned CT-LiPro model in the internal validation set.

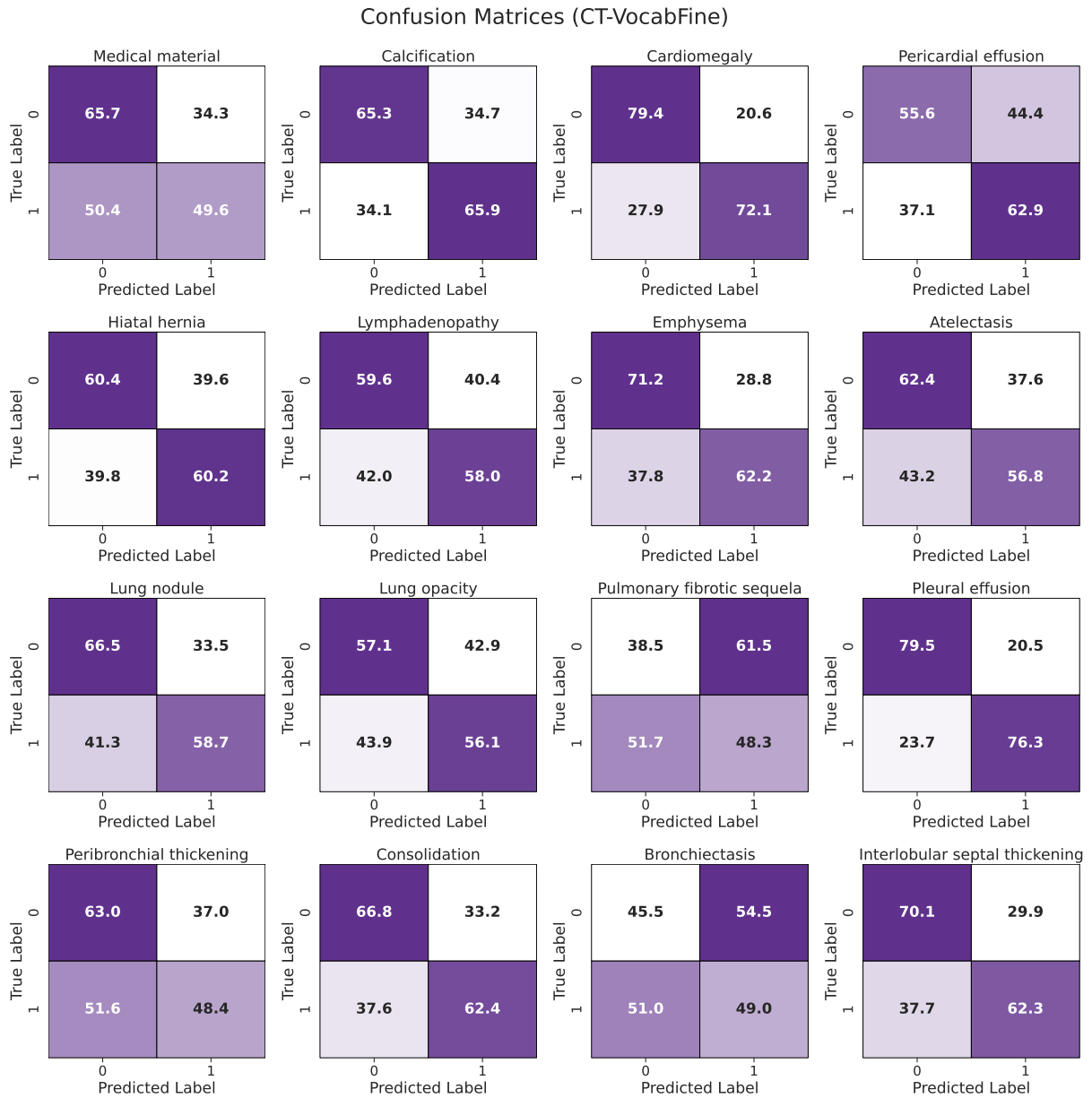




**Supplementary Figure 6: Illustration of confusion matrices for the fully supervised baseline model in the external validation set.**



**Supplementary Figure 7: Illustration of confusion matrices for the zero-shot CT-CLIP model in the external validation set.**



**Supplementary Figure 8: Illustration of confusion matrices for the fine-tuned CT-VocabFine model in the external validation set.**



**Supplementary Figure 9: Illustration of confusion matrices for the fine-tuned CT-LiPro model in the external validation set.**